

# TOPOLOGICAL FLOW DATA ANALYSIS FOR TRANSIENT FLOW PATTERNS: A GRAPH-BASED APPROACH

TAKASHI SAKAJO, TAKESHI MATSUMOTO, SHIZUO KAJI, TOMOO YOKOYAMA,  
AND TOMOKI UDA

**ABSTRACT.** We introduce a time-series analysis method for transient two-dimensional flow patterns based on Topological Flow Data Analysis (TFDA), a new approach to topological data analysis. TFDA identifies local topological flow structures from an instantaneous streamline pattern and describes their global connections as a unique planar tree and its string representation. With TFDA, the evolution of two-dimensional flow patterns is reduced to a discrete dynamical system represented as a transition graph between topologically equivalent streamline patterns. We apply this method to study the lid-driven cavity flow at Reynolds numbers ranging from  $Re = 14000$  to  $Re = 16000$ , a benchmark problem in fluid dynamics data analysis. Our approach reveals the transition from periodic to chaotic flow at a critical Reynolds number when the reduced dynamical system is modelled as a Markov process on the transition graph. Additionally, we perform an observational causal inference to analyse changes in local flow patterns at the cavity corners and discuss differences with a standard interventional sensitivity analysis. This work demonstrates the potential of TFDA-based time-series analysis for uncovering complex dynamical behaviours in fluid flow data.

## 1. INTRODUCTION

Investigations of fluid dynamics are not complete when we finish collecting data on the flow field, such as the velocity, pressure, vorticity and so forth. To describe and understand the rich behaviours of a flow in a given condition, we need to find a structure in the data. Some structures are easily caught by our eyes, like a vortex sheet or tube, which can be highlighted by certain visualization methods in laboratory experiments or numerical simulations. A hairpin vortex in the boundary layer turbulence is a primary example of those structures that lead to the current understanding of the turbulence, see e.g., Davidson [2015]. However, finding a relevant structure of a given flow is hard in general. Moreover finding a reduced-order model of the flow with respect to the elements of the structure is even harder. For the reduced-order modelling, the Galerkin projection with handful terms of the known governing equation has been a systematic tool. The data-driven approaches without needing to know the governing equation include so-called proper orthogonal decomposition (POD) and dynamic mode decomposition (DMD), as explained in Brunton and Kutz [2022] for instance.

Topological Data Analysis (TDA) is a relatively new method describing the topological features of data. See an introductory book by Edelsbrunner and Harer [2010] and an advanced book by Dey and Wang [2022]. While TDA applications in fluid dynamics have gained attention in recent years, concrete examples of its implementation remain limited. In the present paper, we construct a reduced model

of the temporal evolution of streamline patterns using a different TDA approach, called Topological Flow Data Analysis (TFDA), that focuses on the topology of instantaneous streamline patterns of two-dimensional flows. Through this model, we quantitatively track the temporal changes in the topological features of the flow field and analyse the causal relationships between local flow structures by treating pattern transitions as a discrete dynamical system on the reduced model. We thus discuss both the effectiveness of this method and its potential for future development.

The mathematical background behind the TFDA is explained as follows. Let  $\psi(\mathbf{x})$  be a streamfunction of  $C^r$ -class ( $r \geq 1$ ) on a two-dimensional domain  $\mathcal{D} \subset \mathbb{R}^2$ . Since the vector field is defined by  $\mathbf{u} = -\nabla^\perp \psi$  with  $\nabla^\perp = (\partial_y, -\partial_x)$ , it is regarded as a Hamiltonian vector field with  $\psi$  being its Hamiltonian function. Let  $O(\mathbf{x}_0)$  denote a particle orbit advected by the vector field  $\mathbf{u}(\mathbf{x})$  starting from  $\mathbf{x}_0 \in \mathcal{D}$ . That is to say,  $O(\mathbf{x}_0) = \{\phi(s; \mathbf{x}_0) \mid s \in \mathbb{R}\}$ , where  $\phi(s; \mathbf{x}_0)$  is the unique solution to the initial value problem  $\dot{\phi}(s) = \mathbf{u}(\phi(s))$  and  $\phi(0) = \mathbf{x}_0$ . When the vector field is stationary, the particle orbit is contained in a level curve of the streamfunction  $\psi$  owing to  $\nabla\psi \cdot \mathbf{u} = 0$ . A mathematical theory for classifying topological features of the set of all particle orbits,  $\mathcal{O} = \{O(\mathbf{x}_0) \mid \mathbf{x}_0 \in \mathcal{D}\}$ , have been developed by Yokoyama and Sakajo [2013], Sakajo and Yokoyama [2018]. The topological classification is realised under the restrictions of Poincaré–Bendixson theorem, which gives a classification of fixed points, periodic orbits, and limit orbits as  $s \rightarrow \pm\infty$ , and Poincaré–Hopf theorem, which defines the relationship between the index of the vector field and the Euler characteristic of the flow domain. Based on the theory, it is shown in Uda et al. [2019] that the topological structure of particle orbits in  $\mathcal{O}$  is converted uniquely into a discrete graph, named a partially Cyclically Ordered rooted Tree (the abbreviation *COT* is used in this paper), and its string expression, called *COT representation*. Through this transformation, the topological patterns of flow streamlines are represented as graphs or strings, which we call Topological Flow Data Analysis (TFDA). It can also describe the evolution of complex flow patterns as a discrete dynamical system of trees, which gives rise to a reduced-order model of complex flow evolution in terms of topology, as we will demonstrate in this paper. Note that TFDA was originally developed for Hamiltonian vector fields as above, but it has been extended to two-dimensional compressible vector fields recently [Sakajo and Yokoyama, 2022].

TFDA has been applied to a variety of fluid mechanical problems. In Sakajo et al. [2014], TFDA was used to analyse boundary-layer separations around a flat plate with the chord-length based Reynolds number 1370 and the angle of attack  $15^\circ$  in a numerical simulation of a two-dimensional flow. It was shown that the dynamical process was described with brief COT representations. In Uda et al. [2021], TFDA was employed to detect an atmospheric blocking phenomenon, a long-lived high-pressure region blocking the westerly jet flow in the surrounding region, with a year-long observational data in the synoptic scale (over 1000 km). It was confirmed that the method of TFDA outperformed other existing methods for detecting the blocking and that morphological types of the blocking were identified with the COT representations in accordance with the meteorologists' empirical classifications. Sakajo et al. [2022] considered Kuroshio Large Meander in oceanography, which is an abnormal current that gives rise to the entrapment of a cool cyclonic eddy that has substantial impacts on fishery and marine transport. TFDA

is applied to sea surface height data to detect the occurrence of the abnormal state. Furthermore, in Sakajo and Itatani [2023], TFDA has been utilised to classify flow patterns in the left ventricle of the human heart. Actual measurement data with an echocardiography (two spacial dimensions and time) and magnetic resonance imaging (a slice of three spacial dimensions and time) were analysed. Specifically, one can define a swirling flow domain as a topological vortex structure using the COT representations, and it was demonstrated that differences in the flow patterns between normal and diseased hearts were resolved objectively with topological vortex structures in agreement with diagnoses of experienced cardiovascular surgeons.

In these applications mentioned above, TFDA was mainly used to state identifications of flow patterns with vortex-like flow structures, but methods for characterizing the dynamics of transient flow patterns using TFDA have not yet been fully developed. Therefore, in this paper, we propose a new time-series analysis based on TFDA to describe the complex dynamics exhibited by transient flow patterns using a graph-theoretic approach. Our target flow is simple and prototypical: the two-dimensional lid-driven cavity flow [Shen, 1991]. It is perhaps the most famous benchmark problem in computational fluid mechanics when the flow is in a nonlinear steady-state consisting of several corner eddies and one big central eddy. The flow is also regarded as a representative example of the complexity of recirculating eddy and flow separation in a textbook [Ruban and Gajjar, 2013]. Those eddies are explicitly expressed in the COT representation, as we will see later. This means that the tree representation obtained via TFDA is always interpretable in contrast to, for example, the singular vectors of POD and DMD, which are not always easy to interpret. In particular, we demonstrate the capability of TFDA by applying it to the numerical lid-driven cavity flow with the transitional range of Reynolds numbers from time-periodic states to chaotic states.

The paper is constructed as follows. In Section 2, after reviewing the lid-driven cavity flow and the numerical methods to compute it, we provide how we apply TFDA to the lid-driven cavity flows. Section 3 provides numerical results of the time-series analysis proposed in this paper. In Section 3.1, we first describe how snapshots of streamline patterns in the lid-driven cavity flow are converted into COT and COT representations at a moderate Reynolds number. We then show that the evolution of the cavity flow is expressed as a hopping transition among a couple of the COT representations, which is visualised as a network among the COT representations as nodes. This leads to a discrete reduced-order dynamical model of the lid-driven cavity flow. In Section 3.2, we demonstrate that the transition from the periodic state to the chaotic state over Reynolds numbers corresponds to a complication of the network. This hopping picture yields a transition matrix among the tree representations by assuming that the hopping is Markovian. We then utilise a discrete graph analysis to transition matrices to characterize the evolution of flow patterns. Furthermore, to take advantage of the high interpretability of TFDA, we perform an observational causal analysis based on the time series of the tree representation, which is known as the convergent cross mapping (CCM) developed by Sugihara et al. [2012]. Namely, we address which corner eddy is more causal than the other one. We show that the observational CCM approach based on TFDA detects a geometric causality between topological changes in the chaotic flow patterns that the standard sensitivity analysis cannot capture as shown in Appendix A. Discussion and concluding remarks are in Section 4.

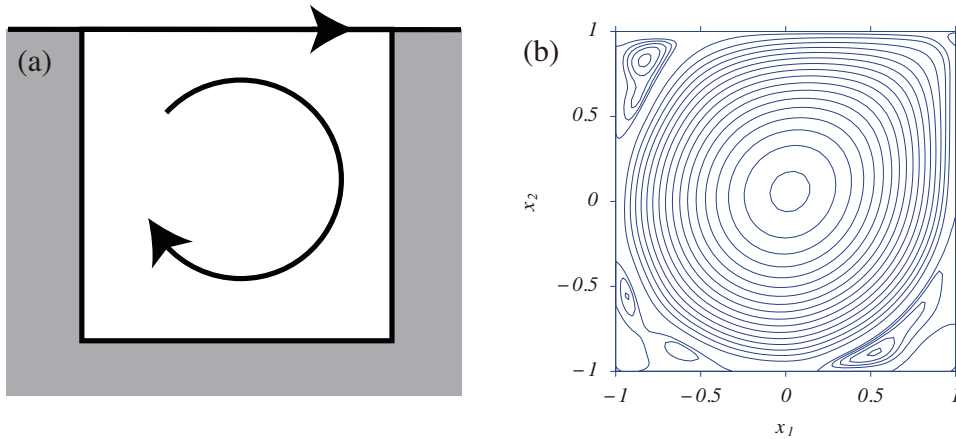


FIGURE 1. (a) The lid-driven cavity flow. (b) A snapshot of a streamline pattern in the cavity.

## 2. OUR TARGET AND METHOD

**2.1. Physics of the lid-driven cavity flow.** The lid-driven cavity flow is a viscous flow in a hollow space enclosed by no-slip walls. The shape of the cavity is usually set to a rectangle in two spatial dimensions and to a rectangular cuboid in three dimensions. One of the walls, the lid, moves with a constant velocity and other walls stay still (zero velocity) as shown in Figure 1(a). As the energy constantly injected by the lid is dissipated by the viscosity, the flow reaches a variety of states depending on the Reynolds number as reviewed in Shankar and Deshpande [2000]. For low Reynolds numbers, the flows are stationary. In other words, they are non-linearly stationary solutions to the Navier-Stokes equations with the given boundary condition. Those stationary solutions, in particular two-dimensional ones, serve as a standard benchmark for numerical methods, see e.g., Ghia et al. [1982] and Botella and Peyret [1998]. As we increase the Reynolds number, the flow becomes time-periodic and then turbulent [Shankar and Deshpande, 2000].

A fundamental fluid-dynamical characteristic of the lid-driven cavity flow, whether it is stationary, periodic or turbulent, is the formation of recirculating eddies at the corners, as emphasized by Ruban and Gajjar [2013]. This phenomenon is illustrated in Figure 1(b), which shows the streamfunction of a stationary solution. In non-stationary flows, the separation and merger of these eddies and boundary layers become important. As Shankar and Deshpande [2000] notes, the lid-driven cavity flow exhibits the full spectrum of fluid mechanical phenomena within the simplest geometrical configuration. This naturally raises the question: how can we systematically understand the flow variations and transitions through the dynamics of these prominent eddies? As we will show in this paper, TFDA provides a systematic and mathematically rigorous framework to achieve this goal for dynamic flow evolutions.

We consider a two-dimensional lid-driven cavity flow in a square cavity. The movement of the lid is regularised around the corners. We adopt the regularisation

proposed in Shen [1991]. Such a regularisation may not be necessary if the corner singularities are properly treated [Batchelor, 1967, Botella and Peyret, 1998, Shankar and Deshpande, 2000]. Our adoption of regularisation is for the sake of numerical simplicity. We specifically consider the incompressible Navier–Stokes equations,

$$(1) \quad \partial_t \mathbf{u} + (\mathbf{u} \cdot \nabla) \mathbf{u} = -\nabla p + \nu \nabla^2 \mathbf{u}, \quad \nabla \cdot \mathbf{u} = 0,$$

in the square domain  $\Omega = \{(x, y) \in \mathbb{R}^2 \mid -1 \leq x \leq 1, -1 \leq y \leq 1\}$ . Hence the side length of the square is  $L = 2$ . Here  $\mathbf{u}(x, y, t)$  is the velocity field,  $p$  is the pressure and  $\nu$  is the kinematic viscosity. The fluid density is normalised to one. The boundary condition is  $\mathbf{u} = \mathbf{0}$  on the boundary walls, except for the lid at the top. The velocity of the lid is given by

$$(2) \quad u(x, y = 1, t) = (x + 1)^2(x - 1)^2,$$

$$(3) \quad v(x, y = 1, t) = 0$$

where  $u(x, y, t)$  and  $v(x, y, t)$  are the  $x$  and  $y$ -components of the velocity [Shen, 1991]. Note that the velocity of the lid becomes zero smoothly at the corners ( $x = \pm 1$ ). The Reynolds number here is defined with the maximum velocity of the lid,  $U = \max_{-1 \leq x \leq 1} u(x, y = 1, t) = 1$ , and the side length of the square,  $L = 2$ , as

$$(4) \quad Re = \frac{UL}{\nu}.$$

The numerical scheme we use is the Chebyshev-tau method in the streamfunction and vorticity formulation of the Navier-Stokes equations. We use the 3/2 rule to remove the dealiasing error. The number of Gauss–Lobatto collocation points is  $65^2$ . The boundary condition is numerically satisfied by using the influence matrix method [Peyret, 2002]. Because of the well-known loss of the rank of the influence matrix, we need to set the vorticity to zero at four collocation points on the boundary (in addition to the corner points). We follow the choice of the four points proposed in Ehrenstein and Peyret [1989], namely the nearest collocation points to the corner points on the lid and bottom wall. The time marching scheme is semi-implicit. Specifically, we use the second-order Adams-Bashforth method for the nonlinear term and the second-order backward differentiation for the viscous term, which is known as AB/BDI2 scheme [Peyret, 2002]. The time-step value is  $\Delta t = 1.0 \times 10^{-3}$ .

We numerically simulate the flow for Reynolds numbers from  $Re = 14000$  to  $Re = 16000$  in steps of 50. For each  $Re$ , we start the simulation with the zero velocity field and continue it up to time  $T_s \gg 1$  when the flow reaches a statistically stationary state to avoid initial transients. Then we start to analyse the flow for  $T_s \leq t \leq T_s + \tilde{t}$ . Their values are  $T_s = 5000 = 2500(L/U)$  and  $\tilde{t}$  varying from  $200 = 100(L/U)$  to  $10000 = 5000(L/U)$ . In Table 1, we list numerical parameters for three representative Reynolds numbers. The convergence study is done for  $Re = 15000$  and  $Re = 16000$  by increasing the collocation points to  $129^2$  or  $257^2$  and halving the time step  $\Delta t$  to check that the results do not change.

As a global fluid mechanical quantity, we consider the kinetic energy

$$(5) \quad E(t) = \int_{\Omega} \frac{1}{2} |\mathbf{u}(x, y, t)|^2 dx dy,$$

and use it as an indicator of the state of the flow as in Shen [1991]. We show the variation of the kinetic energy in Figure 2 and its power spectral density (PSD)

$Re$	collocation points	$\Delta t$	State [Shen, 1991]	State (present)
14000	$65^2$	$1 \times 10^{-3}$	periodic	periodic
15500	$65^2$	$1 \times 10^{-3}$	quasi-periodic	quasi-periodic
16000	$65^2$	$1 \times 10^{-3}$	N/A	chaotic

TABLE 1. Numerical parameters and flow states for representative Reynolds numbers.

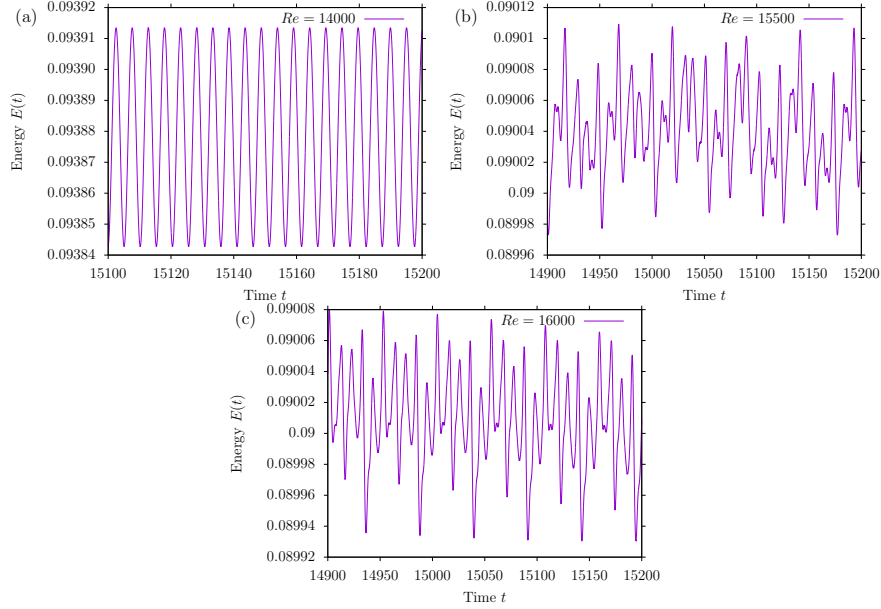


FIGURE 2. The kinetic energy as a function of time for the three representative Reynolds numbers for (a)  $Re = 14000$ , (b)  $Re = 15500$ , and (c)  $Re = 16000$ .

in Figure 3. The PSD for  $Re = 14000$  indicates that the flow is periodic. For  $Re = 15500$ , Shen [1991] concluded that the flow is quasi-periodic. The PSD shown in Figure 3(b) is consistent with the conclusion. For  $Re = 16000$ , the PSD becomes broad and the fine structures seen at  $Re = 15500$  are swallowed by the broad parts. This indicates that the flow is chaotic at  $Re = 16000$ .

**2.2. Topological Flow Data Analysis.** We provide a brief review of TFDA used in this paper. For a complete description of the theory, see Yokoyama and Sakajo [2013], Sakajo and Yokoyama [2018], Uda et al. [2019]. Let us consider a Hamiltonian vector field of  $C^r$ -class ( $r \geq 1$ ) in a two-dimensional disk  $\mathcal{D}$  satisfying the slip boundary condition. Then the particle orbits generated by this Hamiltonian vector field coincide with the level curves of the Hamiltonian function on  $\mathcal{D}$ . Since the streamfunction of the two-dimensional incompressible vector field is the Hamiltonian function of the flow, the level curves are called streamlines. In general, since the vector field can depend on time, the particle orbits advected by the vector field are no longer equivalent to the level curves of the Hamiltonian function. However,

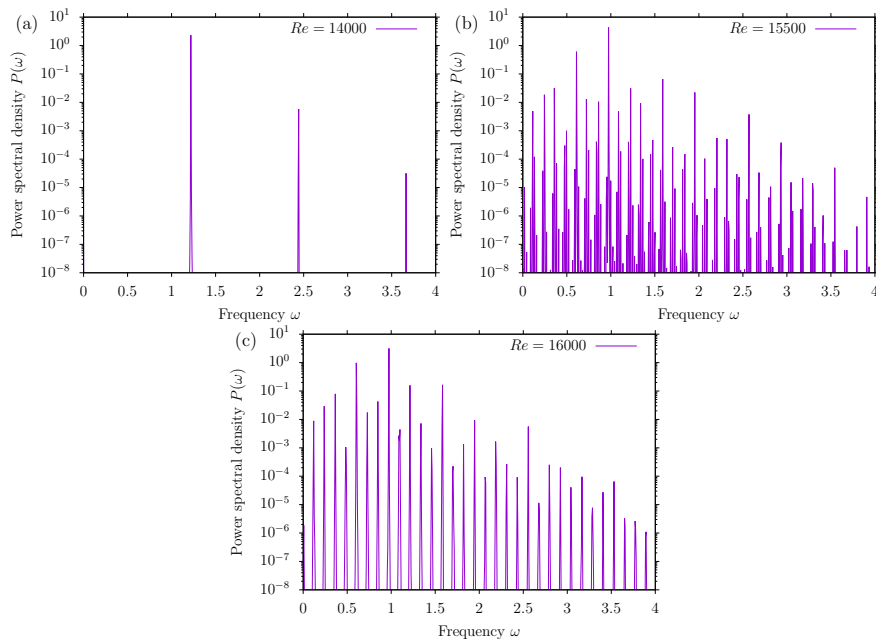


FIGURE 3. Power spectral densities of the kinetic energy for the three representative Reynolds numbers. (a)  $Re = 14000$ , (b)  $Re = 15500$ , and  $Re = 16000$ . The width of the bins for the frequency is the same for the three cases. The densities are calculated from the energy  $E(t)$  in  $5200 \leq t \leq 15200$  in the step of 0.01.

TFDA deals with instantaneous velocity fields and their generating particle orbits, i.e., streamlines, for every fixed time.

Here, we restrict our attention to a special class of the vector field, called *structurally stable* Hamiltonian vector fields. By structural stability, we mean that the topological structure of particle orbits is unchanged under any small perturbation in the  $C^r$  topology. See Ma and Wang [2005], Yokoyama and Sakajo [2013] for a mathematically rigorous definition of structural stability. The set of structurally stable Hamiltonian vector fields in the disk  $\mathcal{D}$  is denoted by  $\mathcal{H}^r$ . Such restriction gives rise to no serious problems theoretically since  $\mathcal{H}^r$  is a generic subset of the set of all  $C^r$  Hamiltonian vector fields. That is to say, any Hamiltonian vector field is approximated by a sequence of structurally stable Hamiltonian vector fields in  $\mathcal{H}^r$ . In addition, practically, numerical simulation of flows mostly generates structurally stable streamline patterns since it hardly resolves structurally unstable orbits due to numerical approximation errors.

To describe the theory of TFDA, we introduce all local orbit structures that appear in structurally stable Hamiltonian flows in  $\mathcal{D}$ . We then provide a unique letter, called a *COT symbol*, to each local orbit structure. Figure 4(a) shows a figure-eight orbit structure with two self-connected saddle connections. To these local orbit structures, we assign the COT symbols  $b_{++}$  and  $b_{--}$ , in which the subscript  $\pm$  indicates the direction of the two self-connected saddle connections. Namely, we use the subscript  $+$  for the saddle connection in the anti-clockwise direction and

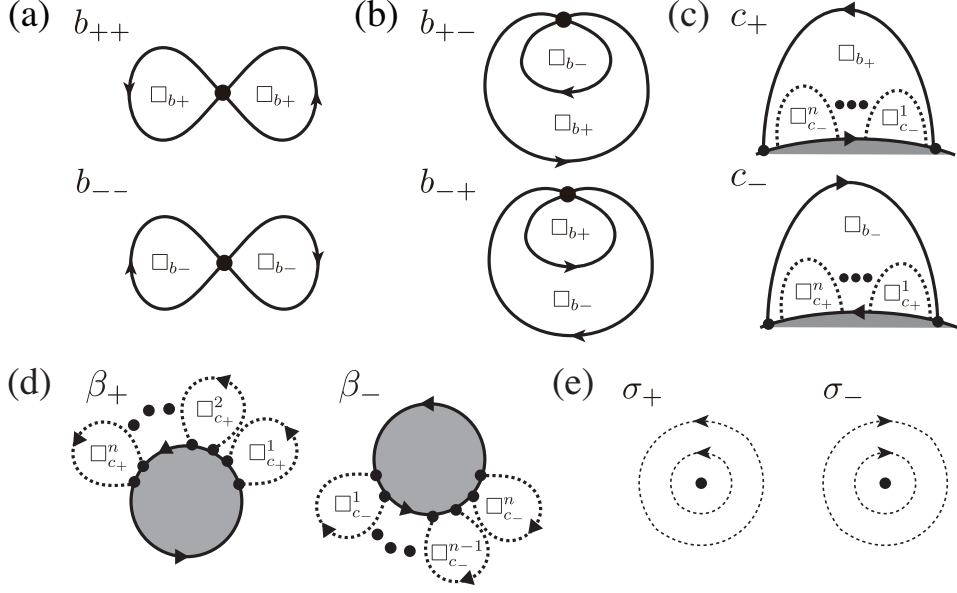


FIGURE 4. Local orbit structures appearing in the streamline patterns of structurally stable Hamiltonian vector fields in  $\mathcal{D}$ . (a) Figure-eight patterns with a saddle and two self-connected saddle separatrices whose COT symbol is  $b_{\pm\pm}$ . (b) Local orbit structures with a saddle, in which one saddle connection encloses another. The COT symbol is  $b_{\pm\mp}$ . (c) Saddle connections between two different saddles on the same boundary. The COT symbol is  $c_{\pm}$ . (d) Isolated boundaries,  $\beta_{\pm}$ . (e) Elliptic centres,  $\sigma_{\pm}$ . In each panel,  $\square_{b_{\pm}}$  and  $\square_{c_{\pm}}$  indicate that the local orbit structures in (6) are embedded in the flow structures as their internal structure.

the subscript  $-$  for the clockwise one. We have other local orbital structures as in Figure 4(b) consisting of a saddle and two self-connected saddle connections, in which one saddle connection surrounds another. Since the flow directions along the saddle connections become the opposite, its COT symbol is given by  $b_{\pm\mp}$ . Figure 4(c) shows local orbit structures consisting of a saddle connection between two different saddles on the same boundary. The COT symbol  $c_{\pm}$  is assigned to the structures according to the orientations of the saddle connections. We further consider an isolated boundary along which the flow is going in the anti-clockwise (resp. clockwise) direction in Figure 4(d). The COT symbol is given by  $\beta_{+}$  (resp.  $\beta_{-}$ ). The box symbols  $\square_{b_{\pm}}$  and  $\square_{c_{\pm}}$  in Figure 4(a–d) express that local orbit structures are embedded as internal structures there. In other words, each box symbol corresponds to a local orbit structure chosen as

$$(6) \quad \square_{b_{\pm}} \in \{b_{\pm\pm}, b_{\pm\mp}, \sigma_{\pm}, \beta_{\pm}\}, \quad \square_{c_{\pm}} \in \{c_{\pm}\}.$$

For instance, in the local orbit structures of  $c_{\pm}$  in Figure 4(c), the saddle connection needs to enclose one local orbit structure from (6) in  $\square_{b_{\pm}}$  as an internal structure. On the other hand, one can attach any number of the local orbit structures  $\square_{c_{\pm}}^i$  ( $i = 1, \dots, n$ ) at regions enclosed by dashed curves along the boundary, but these



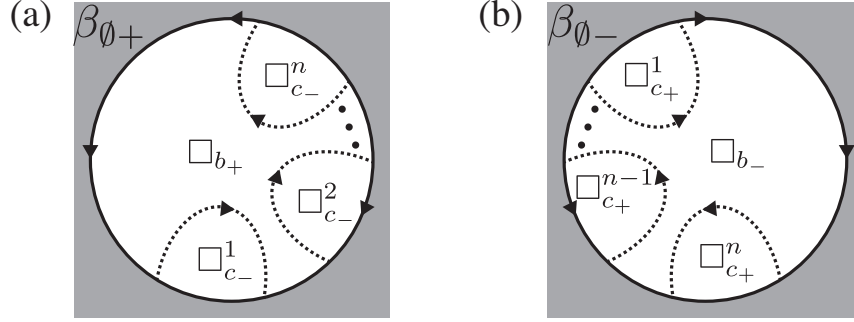


FIGURE 5. Root structures in the disk  $\mathcal{D}$ , where a local orbit structures  $b_{\pm\pm}$  or  $b_{\pm\mp}$  can be embedded and any number of  $c_{\pm}$  structures are attached to the boundary of the disk. (a) The root structure  $\beta_{\theta+}$ . The flow along the boundary is going in the anti-clockwise direction. (b) The root structure  $\beta_{\theta-}$ . The flow along the boundary is going in the clockwise direction.

structures are not necessarily present, i.e.  $n = 0$  is allowed. The same situation also applies to the structure  $\beta_{\pm}$ . Finally, we define an isolated elliptic centre whose COT symbol is  $\sigma_+$  (resp.  $\sigma_-$ ) associated with anti-clockwise (resp. clockwise) periodic orbits in Figure 4(e). Note that they have no internal structures.

For the topological orbit structures generated by structurally stable Hamiltonian vector fields in  $\mathcal{D}$ , the following result has been shown by Yokoyama and Sakajo [2013].

**Theorem 1.** *The topological structure of particle orbits (streamlines) generated by structurally stable Hamiltonian vector field in  $\mathcal{D}$  is uniquely represented by a combination of the local orbit structures  $b_{\pm\pm}$ ,  $b_{\pm\mp}$ ,  $c_{\pm}$ ,  $\sigma_{\pm}$  and  $\beta_{\pm}$ .*

Based on the classification theorem, we convert the topological structure of orbit connections for a given structurally stable Hamiltonian vector field in  $\mathcal{D}$  into a planar tree and its string expression, which are the output of TFDA. The conversion algorithm is outlined as follows. For a detailed description of the algorithm, refer to Uda et al. [2019]. Let us first consider two topologically simplest flows in the disk  $\mathcal{D}$  as shown in Figure 5, which are called the root structures. When the flow direction along the boundary of the disk is anti-clockwise (resp. clockwise), we assign the COT symbol  $\beta_{\theta+}$  (resp.  $\beta_{\theta-}$ ). They indicate that the root structure contains at least one local orbit structure in  $\square_{b_{\pm}}$  and any number of local orbit structures at  $\square_{c_{\pm}}$  can be attached along the boundary. Next, for the given structurally stable Hamiltonian vector field (or the Hamiltonian function), starting from the root structures, we identify the internal local orbit structures corresponding to  $\square_{b_{\pm}}$  and  $\square_{c_{\pm}}$  inductively. Every time we identify internal local orbit structures, we create an edge from the parent node of the structure containing them to the child nodes of embedded internal local structures. Repeating this step inductively until we reach isolated elliptic centres or boundaries with no  $c_{\pm}$  structures attached yields a planer tree, namely a partially Cyclically Ordered rooted labelled Tree (COT). According to Sakajo and Yokoyama [2018], it has been mathematically shown that if the root node is fixed, COTs are in one-to-one correspondence with the topological orbit

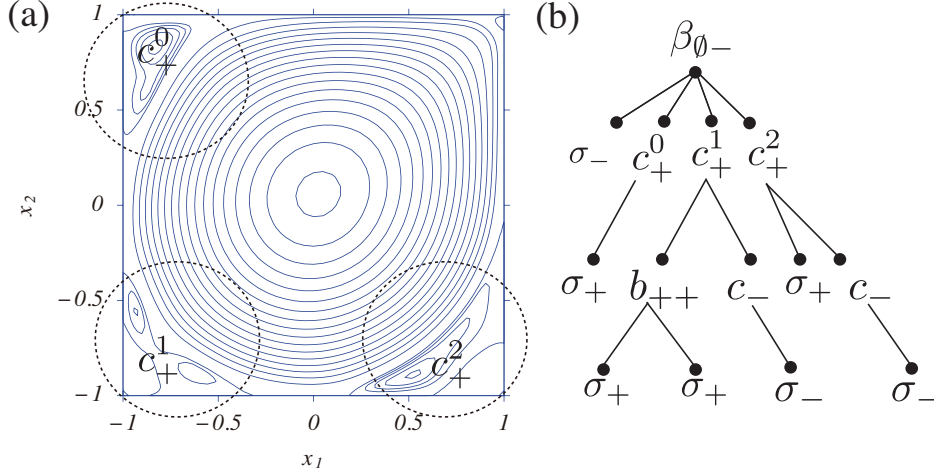


FIGURE 6. (a) A snapshot of the streamline pattern of the lid-driven cavity flow at Reynolds number  $Re = 14000$ . (b) The partially cyclically ordered labelled rooted tree (COT) of the streamline pattern, whose COT representation is given by (7).

structures of structurally stable Hamiltonian vector fields. This means that a COT becomes a unique identifier of the flow pattern in terms of topology. Remark that the COT is equivalent to the Reeb graph of the streamfunction [Uda et al., 2019]

**2.3. TFDA for the lid-driven cavity flow.** As an example, we explain how the conversion algorithm is applied to an instantaneous streamfunction in the lid-driven cavity at  $Re = 14000$  in Figure 6(a). The flow inside the cavity can be regarded as a Hamiltonian flow in a bounded region inside a rectangle. This is because the value of the streamfunction becomes a constant along the boundary of the cavity and a level curve of the same value in the open part above the lid also closes this rectangular region. Hence, the flow is topologically equivalent to a structurally stable Hamiltonian flow in the disk  $\mathcal{D}$ , to which the conversion algorithm is applicable.

Since the flow goes around the boundary of the cavity in the clockwise direction, the root structure of this flow is identified as  $\beta_{\theta-}$  as in Figure 5(b). As an internal structure of the cavity flow corresponding to  $\square_{b-}$  of the root structure  $\beta_{\theta-}$ , we identify an elliptic centre  $\sigma_-$  located at the centre of a large rotating flow region. For orbit structures of  $\square_{c+}$  along the boundary, we find three local orbit structures  $c_+$  in Figure 4(c) connecting between saddles on the boundary at the corners of the cavity. These orbit structures express the existence of the recirculating regions. Here, to distinguish these  $c_+$  structures, we assign the enumerated COT symbols  $c_+^0$ ,  $c_+^1$ , and  $c_+^2$  to the recirculating regions the top left corner, the bottom left corner, and the bottom right corner respectively, as shown in Figure 6(a). Since the elliptic centre  $\sigma_-$  and the three  $c_+$  structures are identified as the internal structures contained in the root structure  $\beta_{\theta-}$ , we create the root node of  $\beta_{\theta-}$  and four child nodes of the local orbit structures  $\sigma_-$  and  $c_+^i$  for  $i = 0, 1, 2$ , and we then connect them with edges. Since the elliptic centre  $\sigma_-$  in the centre of the rotating region has no internal structure, we stop the procedure for this node.

Similarly, since only elliptic centres  $\sigma_+$  are contained in the orbit structure  $c_+^0$ , the procedure stops after adding the node of the elliptic centre with the label  $\sigma_+$  as its child node. On the other hand, since an anti-clockwise figure-eight  $b_{++}$  structure in Figure 4(a) is contained inside the  $c_+^1$  structure at the bottom left corner, a new node with label  $b_{++}$  is created as a child node and an edge connecting to the parent node with the label  $c_+^1$ . Both recirculating domains  $c_+^1$  and  $c_+^2$  contain a small recirculating domain  $c_-$  inside, where the flow is rotating in the opposite direction. Finally, there are isolated elliptic centres  $\sigma_+$  inside the orbit structure  $b_{++}$  and  $\sigma_-$  inside the structure  $c_-$ , so the conversion algorithm terminates. As a result, we obtain the COT as shown in Figure 6(b) expressing the topological structure of the streamline pattern.

The COT is expressed as a sequence of COT symbols, say COT representation, which is given by

$$(7) \quad \beta_{\emptyset-}(\sigma_-, c_+^0(\sigma_+)) \cdot c_+^1(b_{++}\{\sigma_+, \sigma_+\}, c_-(\sigma_-)) \cdot c_+^2(\sigma_+, c_-(\sigma_-)).$$

It is obtained by using a regular tree grammar with cyclic order introduced in Yokoyama and Yokoyama [2020], which is a generalization of the regular tree grammar (cf. Comon et al. [2008]). The specific implementation procedure for the grammar, which is a theoretical conversion rule, is described in Uda et al. [2019]. Since we use the COT symbols as the labels of the nodes of the tree, we refer to the local orbit structures with the COT symbols in the COT representations.

We perform our TFDA calculations using `psiclone`, a Python library that implements the algorithm computing COT representations developed by Uda et al. [2019]. First, given a grid dataset representing a streamline function  $\psi$ , we compute the persistent homologies of sublevel and superlevel filtrations of  $\psi$ . The adjacency structure of the data grid is assumed to follow the von Neumann neighbourhood (4-neighbourhood). Given a prescribed threshold value  $\varepsilon > 0$ , we discard intervals (or bars) in both persistent homologies whose lifetimes (or lengths) are less than  $\varepsilon$ . In our analysis, we set the threshold value to  $\varepsilon = 5.0 \times 10^{-4}$ , chosen to ignore small-scale variations of the streamfunction, particularly those near the boundary of the computational domain. Second, we combine both persistent homologies and obtain the Reeb graph of  $\psi$ , which provides a global topological summary of the nesting information of the streamlines. Third, we scan all the edges in the Reeb graph and convert their local patterns into nested COT symbols inductively, as described in the previous subsection. Here, since there are multiple choices for the COT root nodes, we fix the choice by selecting the representative root point minimising the streamline function value. That is to say, the scanning of level sets starts from this root point  $\operatorname{argmin} \psi(x, y)$ . After obtaining the COT, we incorporated supplementary information by assigning corner location numbers  $i = 0, 1, 2$  to  $c_+$  in the COT, representing the recirculating flow domains at the top left, bottom left, and bottom right corners, respectively. The enumeration of the COT symbol  $c_+$  for the top right corner is omitted, as the lid-driven cavity configuration does not allow for large-scale local orbit structures in that region. Note that the number of child nodes of type  $c_+$  varies over time, and a corner may have multiple  $c_+$  nodes or none at all.

### 3. NUMERICAL RESULTS

#### 3.1. Detailed analysis at $Re = 14000$ .

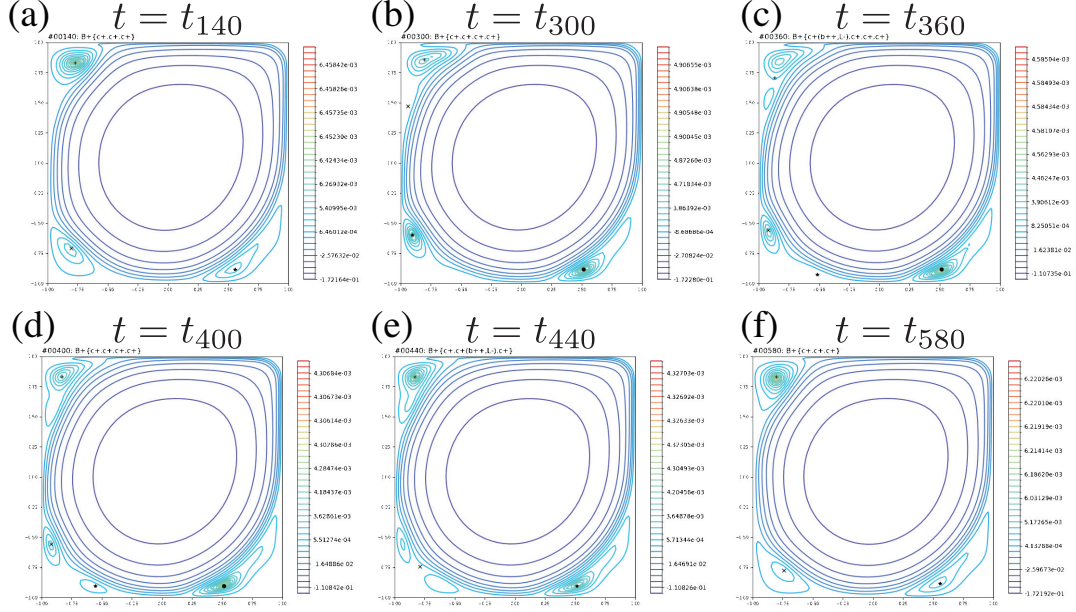


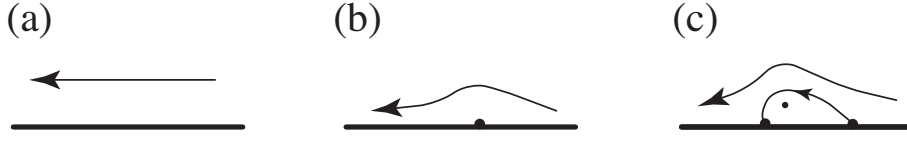
FIGURE 7. Transition of the streamline patterns in the lid-driven cavity flow from  $t = t_{140}$  to  $t = t_{580}$ . The Reynolds number is  $Re = 14000$ .

3.1.1. *Transition of streamline topology.* Considering the lid-driven cavity flow at  $Re = 14000$ , we describe how the topological structures of streamline patterns change by utilising COT representations. While the flow pattern evolves continuously in time, their topological structures remain unchanged for a certain period since they are robust under small continuous perturbations. By TFDA, we show that the evolution of the flow patterns is decomposed into a discrete transition among several topological equivalence classes of flow patterns with the same COT representations. In this analysis, we sample the streamline data every 10 steps after  $t = T_s$ , i.e., at  $t = t_k \equiv T_s + 10(k + 1)\Delta t$  for  $k = 0, 1, \dots$ .

Figure 7 shows snapshots of the evolution of the flow from  $t = t_{140}$  to  $t = t_{580}$ , in which we observe five topologically different flow patterns whose COT representations are provided in Table 2. The COT representation is uniquely provided to flow patterns with the same topological structure, and this state continues for a certain period in the evolution. Hence, each COT representation is associated with a duration as shown in Table 2. For instance, the flow patterns from  $t = t_0$  to  $t = t_{277}$  have the same topological structure as that for Figures 7(a), so the COT representation  $\beta_{0-}(\sigma_-, c_+^0(\sigma_+) \cdot c_+^1(\sigma_+) \cdot c_+^2(\sigma_+))$  remains unchanged in this period. At  $t = t_{278}$ , the topological structure of the flow pattern transitions to the one with the same COT representation as that for Figure 7(b), i.e.,  $\beta_{0-}(\sigma_-, c_+^0(\sigma_+) \cdot c_+^0(\sigma_+) \cdot c_+^1(\sigma_+) \cdot c_+^2(\sigma_+))$ , and it continues until  $t = t_{318}$ . Similarly, we have the duration associated with the COT representations. Hence, the flow patterns in Figure 7 are regarded as the representative elements of the topologically equivalent classes, and the evolution of

Figure	time	COT	duration
7(a)	$t = t_{140}$	$\beta_{\theta_-}(\sigma_-, c_+^0(\sigma_+) \cdot c_+^1(\sigma_+) \cdot c_+^2(\sigma_+))$	$[t_0, t_{277}]$
7(b)	$t = t_{300}$	$\beta_{\theta_-}(\sigma_-, c_+^0(\sigma_+) \cdot c_+^0(\sigma_+) \cdot c_+^1(\sigma_+), c_+^2(\sigma_+))$	$[t_{278}, t_{318}]$
7(c)	$t = t_{360}$	$\beta_{\theta_-}(\sigma_-, c_+^0(b_{++}\{\sigma_+, \sigma_+\}, c_-(\sigma_-)) \cdot c_+^1(\sigma_+) \cdot c_+^1(\sigma_+) \cdot c_+^2(\sigma_+))$	$[t_{319}, t_{397}]$
7(d)	$t = t_{400}$	$\beta_{\theta_-}(\sigma_-, c_+^0(\sigma_+) \cdot c_+^1(\sigma_+) \cdot c_+^1(\sigma_+) \cdot c_+^2(\sigma_+))$	$[t_{398}, t_{424}]$
7(e)	$t = 440$	$\beta_{\theta_-}(\sigma_-, c_+^0(\sigma_+) \cdot c_+^1(b_{++}\{\sigma_+, \sigma_+\}, c_-(\sigma_-)), c_+^2(\sigma_+))$	$[t_{425}, t_{497}]$
7(f)	$t = 580$	$\beta_{\theta_-}(\sigma_-, c_+^0(\sigma_+) \cdot c_+^1(\sigma_+) \cdot c_+^2(\sigma_+))$	$[t_{498}, t_{580}]$

TABLE 2. The COT representations for the flow patterns in Figure 7.

FIGURE 8. Generation of a local orbit structure represented by  $c_+(\sigma_+)$  through a pinching transition.

the flow patterns is thus reduced to a discrete transition between the COT representations.

Owing to the uniqueness, using the COT symbols contained in the COT representations, we can describe how the topological structure of the flow changes in these periods. Since all the COT representations start from the same COT symbol  $\beta_{\theta_-}$  expressing that the root structure is a large clockwise rotational flow, we pay attention to the local flow structure represented by the sequence of COT symbols inside the parenthesis of  $\beta_{\theta_-}$ . The first COT symbol in the sequence is  $\sigma_-$  in all cases, indicating the existence of an isolated elliptic fixed point at the centre of the large rotational flow. In the COT representation for Figure 7(a) at  $t = t_{140}$ , the three COT symbols  $c_+^i(\sigma_+)$  for  $i = 0, 1, 2$  follows  $\sigma_-$ . Each symbol represents an anti-clockwise recirculating flow region enclosed by a boundary saddle connection at the corner of the cavity. In Figure 7(a), these elliptic centres in the recirculating flow domains are plotted using markers  $+$ ,  $\times$ ,  $\star$ , and  $\bullet$ . At  $t = t_{300}$ , another  $c_+^0(\sigma_+)$  is added to the COT representation for the pattern of Figure 7(b), indicating that a new boundary saddle connection appears at the top left corner. The pair of the COT symbols  $c_+^0(\sigma_+) \cdot c_+^0(\sigma_+)$  in the COT representation at  $t = t_{300}$  is then replaced by  $c_+^0(b_{++}\{\sigma_+, \sigma_+\}, c_-(\sigma_-))$  at  $t = t_{360}$ . This means that the two boundary saddle connections merge and transition to a local orbit structure of a boundary saddle connection containing a figure-eight orbit structure as observed at the top left corner in Figure 7(c). Afterwards,  $c_+^0(b_{++}\{\sigma_+, \sigma_+\}, c_-(\sigma_-))$  is reduced to a simple  $c_+^0(\sigma_+)$  in the COT representation at  $t = t_{440}$ . Hence, the figure-eight orbit structure at the top left corner disappears and transforms into a simple boundary saddle connection as in Figure 7(d). The COT symbol  $c_+^1(\sigma_+)$  at  $t = t_{300}$  similarly changes as  $c_+^1(\sigma_+) \cdot c_+^1(\sigma_+) \rightarrow c_+^1(b_{++}\{\sigma_+, \sigma_+\}, c_-(\sigma_-)) \rightarrow c_+^1(\sigma_+)$  from  $t = t_{360}$  to  $t = t_{580}$ . This also indicates that the local orbit structure at the bottom left corner is subject to the same topological transitions as that at the top left corner. After these transitions occur, the COT representation at  $t = t_{580}$  finally returns the same one at  $t = t_{140}$ .

According to Sakajo and Yokoyama [2015], by observing the changes in the COT symbols, we can theoretically describe generic topological transitions between local flow patterns and specify marginal structurally unstable flow patterns between them. The generation process of a boundary saddle connection  $c_+^0(\sigma_+)$  at the top left corner from  $t = t_{140}$  to  $t = t_{300}$  is schematically provided in Figure 8. From Figure 8(a) to Figure 8(c), a degenerate boundary stagnation point appears on the boundary as in Figure 8(b) and it divides into two regular boundary saddles. This transition is called a *pinching transition*. Note that the flow of Figure 8(b) is hardly observed in the numerical simulation since it is structurally unstable. On the other hand, the transition of the boundary saddle connection at the top left corner from  $t = t_{140}$  to  $t = t_{360}$  is expressed as the following changes in the COT symbols.

$$(8) \quad c_+^0(\sigma_+) \cdot c_+^0(\sigma_+) \longrightarrow c_+^0(b_{++}\{\sigma_+, \sigma_+\}, c_-(\sigma_-)) \longrightarrow c_+^0(\sigma_+).$$

Based on this, we explain the topological transition of the local flow patterns at the top left corner in this period. See Figure 9. From  $t = t_{140}$  to  $t = t_{300}$ , the two boundary saddle connections represented by  $c_+^0(\sigma_+) \cdot c_+^0(\sigma_+)$  in Figure 9(a) approach and a structurally unstable flow pattern with heteroclinic connections emerges as in Figure 9(b). Then a slight perturbation instantaneously gives rise to the transition to a structurally stable pattern with a figure-eight orbit structure as in Figure 9(c). This transition is called a *heteroclinic transition*. The local orbit structure after the heteroclinic transition is represented by the sequence of the COT symbol  $c_+^0(b_{++}\{\sigma_+, \sigma_+\}, c_-(\sigma_-))$ , indicating that a small clockwise recirculating flow region  $c_-(\sigma_-)$  exists inside the boundary saddle connection  $c_+^0$ ; From  $t = t_{300}$  to  $t = t_{360}$ , we need two more steps to complete the transition. The elliptic centres in the figure-eight pattern merge, and the flow pattern transfers to that of Figure 9(d) which is represented by  $c_+^0(\sigma_+, c_-(\sigma_-))$ . This structure then transfers to a simple local orbit structure of  $c_+^0(\sigma_+)$  in Figure 9(f) through a marginal pattern in Figure 9(e) having a degenerate saddle on the boundary. This is another pinching transition. Hence, the theory concludes that the change in the COT symbols of (8).

Although we expect the existence of the structurally stable local flow pattern represented by  $c_+^0(\sigma_+, c_-(\sigma_-))$  as in Figure 9(d) in theory, the height difference of the Hamiltonian function for the internal orbit structure  $c_-(\sigma_-)$  is so small that *psiclone* can cut it off in practice due to the threshold parameter  $\varepsilon$ . There occurs the same transition of the anti-clockwise recirculating region represented by  $c_+^1$  at the bottom left corner from  $t = t_{400}$  to  $t = t_{580}$ .

**3.1.2. Transition diagram of the flow evolution.** As we see in Section 3.1.1, the change of flow patterns from  $t = t_0$  to  $t = t_{580}$  at  $Re = 14000$  is expressed as a cycle of the COT representations of the five topologically equivalent patterns in Table 2. Those COT representations share the same root structure  $\beta_{\theta_-}$  followed by  $\sigma_-$  expressing the large clockwise rotational region in the cavity. Hence, the five topological equivalence classes are distinguished by the sequences of the COT symbols  $c_+^i$  ( $i = 0, 1, 2$ ) to the right of  $\sigma_-$ , which represents the topological structure in the recirculating flow domains at the cavity corners.

We now track the change of the sequences of  $c_+^i$  in the COT representations in the temporal direction as follows. Applying TFDA to the flow pattern at each time, we extract the sequence of  $c_+^i$  in the COT representation. We do nothing as long as this sequence remains the same. When the sequence changes, we create

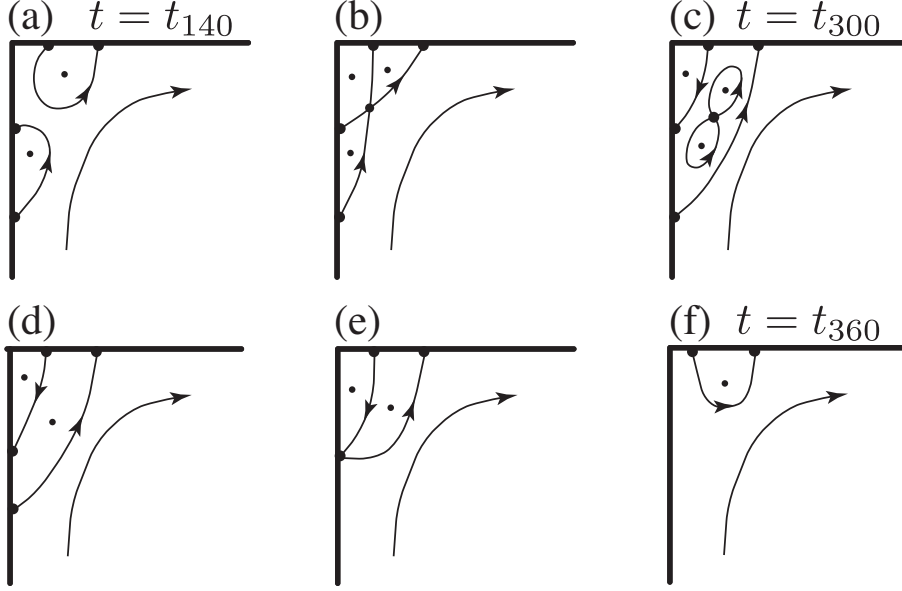


FIGURE 9. Schematic of topological transitions of local flow patterns at the top left corner through marginal structurally unstable patterns. (a) The flow pattern at  $t = t_{140}$  represented by  $c_+^0(\sigma_+) \cdot c_+^0(\sigma_+)$ . (b) A structurally unstable flow pattern with heteroclinic connections. (c) The flow pattern at  $t = t_{300}$  represented by  $c_+(b_{++}\{\sigma_+, \sigma_+\}, c_-(\sigma_-))$ . (d) A structurally stable flow pattern represented by  $c_+(\sigma_+, c_-(\sigma_-))$ , which is expected to exist between the patterns at  $t = t_{300}$  and  $t = t_{360}$  according to Sakajo and Yokoyama [2015]. (e) A structurally unstable flow pattern with a degenerate boundary saddle. (f) The structurally stable pattern at  $t = t_{360}$  represented by  $c_+(\sigma_+)$ .

a directed edge connecting the nodes labelled by the COT sequences before and after the change. Repeating the procedure for the whole evolution, we obtain a directed graph representing the transition between the nodes labelled by the COT sequences. We call this directed graph a *transition diagram*. By creating the transition diagram, we reduce the evolution of the lid-driven cavity flow into a discrete dynamical system among the finite number of topologically equivalent flow patterns. Figure 10(a) is the transition diagram constructed by the flow evolution at  $Re = 14000$  from  $t = t_0$  to  $t_{10000}$ . The label of each node in this diagram represents a sequence of COT symbols. For instance, the label “c+0(b++c-).c+1.c+1.c+2” corresponds to the sequence  $c_+^0(b_{++}\{\sigma_+, \sigma_+\}, c_-(\sigma_-)) \cdot c_+^1(\sigma_+) \cdot c_+^1(\sigma_+) \cdot c_+^2(\sigma_+)$  in the COT representation at  $t = t_{360}$  in Table 2.

In addition, from the transition diagram, we obtain an  $N \times N$  transition matrix  $\mathcal{M}$  between  $N$  nodes as follows. For each node  $i$ , we count the number of transitions to the node  $j$  ( $j \neq i$ ), say  $C_{ij}$ , for  $j = 1, \dots, N$ . Note that  $C_{ii} = 0$  since we do not count the transition from the node  $i$  to itself when constructing the transition

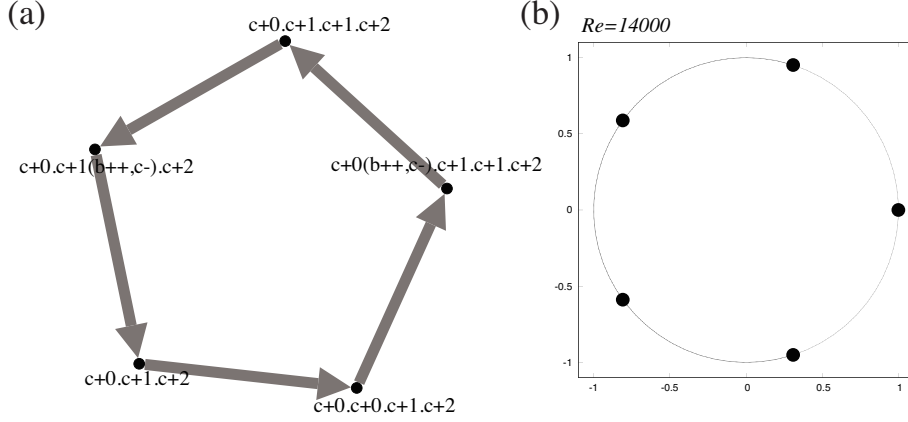


FIGURE 10. (a) Transition diagram for the evolution of the lid-driven cavity flow at  $Re = 14000$ . (b) Plot of the eigenvalues of the transition matrix in the complex plane.

diagram. The entries of  $\mathcal{M}$  are then given by

$$\mathcal{M}_{ij} = \frac{C_{ij}}{\langle C \rangle_i}, \quad \langle C \rangle_i = \sum_{j=1}^N C_{ij}.$$

Then we have  $\sum_{j=1}^N \mathcal{M}_{ij} = 1$  for any  $i$ . The eigenvalues of this transition matrix  $\mathcal{M}$  provide information about the discrete dynamical system as the Markov process on the graph. Let us consider the initial probability distribution  $\mu(0)$  on the graph. Suppose that the transition matrix  $T$  has the distinct eigenvalues  $\lambda_j$  and its associated left eigenvector  $\ell_j$  for  $j = 1, \dots, N$ . Recall that all eigenvalues of the transition matrix exist in the unit disk. Then the probability distribution at time step  $k$  is represented by

$$(9) \quad \mu(k)^T = \sum_{j=1}^m d_j \lambda_j^k \ell_j^T + \sum_{j=m+1}^N d_j \lambda_j^k \ell_j^T$$

with the constants  $d_j$  satisfying  $\mu(0)^T = \sum_{j=1}^N d_j \ell_j^T$ , where  $|\lambda_j| = 1$  for  $j = 1, \dots, m$  and  $|\lambda_j| < 1$  for  $j = m+1, \dots, N$ . The first term represents the persistent dynamics for all time steps, while the second term is the transient part decaying as time proceeds. Figure 10(b) shows the distribution of the eigenvalues of the transition matrix for  $Re = 14000$ . Recall that the transition matrix always has the Perron–Frobenius eigenvalue 1. The other four eigenvalues are located at the vertices of the right pentagon on the unit circle. Hence, the decomposition (9) indicates that this discrete dynamical system is in periodic motion with period five.

## 3.2. Comparison across Reynolds numbers.

3.2.1. *Graph analysis of transition diagram.* We investigate the behaviour of the reduced discrete dynamical system of the lid-driven cavity flow in detail using techniques of discrete graph analysis stated above. Let us consider the range of Reynolds



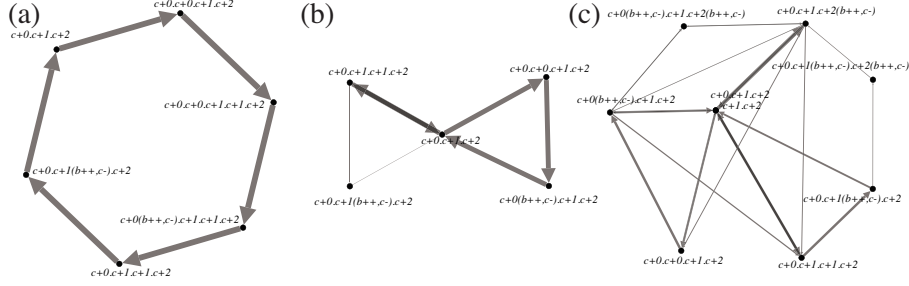


FIGURE 11. Transition diagrams for the lid-driven cavity flow at (a)  $Re = 14500$ , (b)  $Re = 15000$ , and (c)  $Re = 15500$ .

numbers from  $Re = 14000$  to  $Re = 16000$ , where periodic behaviour changes to chaotic aperiodic behaviour according to Shen [1991].

Figures 11(a-c) are the transition diagrams at  $Re = 14500$ ,  $Re = 15000$ , and  $Re = 15500$ , respectively. Figure 12 shows the distributions of the eigenvalues of the transition matrix corresponding to the transition diagrams for various Reynolds numbers. At  $Re = 14500$ , the diagram forms a hexagonal transition among six topologically equivalent flow patterns in one direction. The eigenvalues of the corresponding transition matrix in Figure 12(b) are located at the vertices of the right hexagon on the unit circle, indicating that the motion of the discrete dynamical system is periodic with period six. When the Reynolds number becomes  $Re = 15000$ , the transition diagram in Figure 11(b) consists of two triangles. It suggests that the transitions of the local flow patterns at the recirculating regions  $c_+^0$  and  $c_+^1$  occur alternately. Figure 12(d) shows that the eigenvalues except for the Perron–Frobenius eigenvalue are inside the unit circle. Since the arguments of the two eigenvalues are  $\pm\frac{2}{3}\pi$ , a decaying periodic motion with period three exists. The remaining one is near the origin, indicating the degenerate node “c0.c1.c2” connects the two triangles in the transition diagram. When the Reynolds number gets larger,  $Re = 15500$ , the transition diagram becomes complicated as shown in Figure 11(c). Then we find no eigenvalues generating almost periodic behaviour as shown in Figure 12(f). Hence, we expect the change from periodic motion to aperiodic one between  $Re = 15000$  and  $Re = 15500$ .

To see the complexity of the discrete dynamical system among flow patterns in detail, we refer to the distribution of the eigenvalues for other Reynolds numbers in Figure 12, and the average degree of nodes in the transition diagrams in Table 3. For  $Re = 14250$  (Figure 12(a)) and  $Re = 14500$  (Figure 12(b)), the eigenvalues are on the vertices of the regular hexagon on the unit circle, and the average degrees of the diagrams are approximately 1. Hence, the discrete dynamical systems exhibit periodic motions with period six. At  $Re = 14750$  in Figure 12(c), since the eigenvalues are on the equilateral triangle on the unit circle and at the origin, and

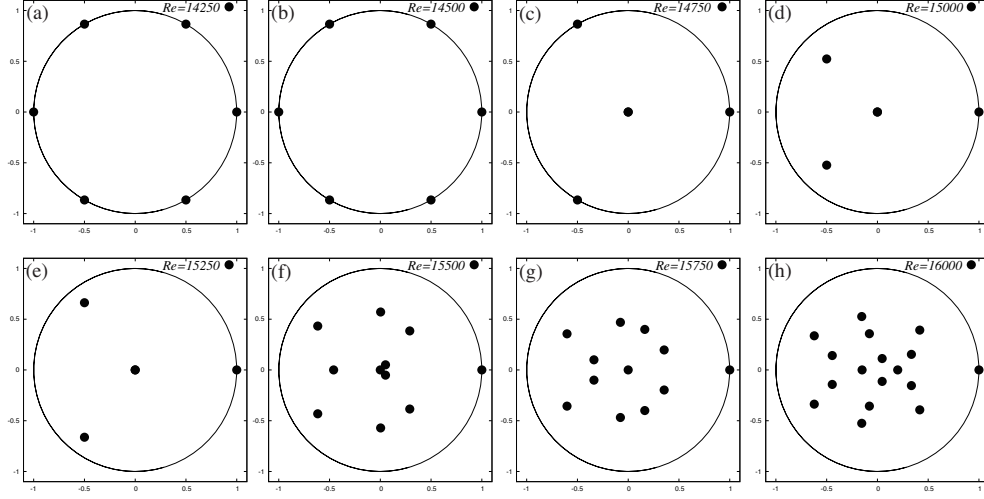


FIGURE 12. Eigenvalues of the transition matrices corresponding to the lid-driven cavity flow in the transition regime of the Reynolds number. (a)  $Re = 14250$ . (b)  $Re = 14500$ . (c)  $Re = 14750$ . (d)  $Re = 15000$ . (e)  $Re = 15250$ . (f)  $Re = 15500$ . (g)  $Re = 15750$ . (h)  $Re = 16000$ .

Reynolds number	14000	14250	14500	14750	15000	15250	15500	15750	16000
Averaged degree	1	1.167	1	1.5	1.4	1.667	2.556	2.4	2.909

TABLE 3. The averaged degree of the transition diagrams in the transition regime.

the average degree is 1.5, the motion of the discrete dynamical system is a three-periodic motion running on the two connected triangular graphs. For  $Re = 15000$  (Figure 12(d)) and  $Re = 15250$  (Figure 12(e)), the discrete dynamical system exhibits a decaying periodic motion with period three. At  $Re = 15500$  or greater, the number of nodes in the transition diagram increases as shown in Figure 12(f-h), since we find many topologically equivalent flow patterns. The eigenvalues other than the Perron–Frobenius eigenvalue are distributed inside the unit circle. The average degree of the transition diagrams also gets larger, indicating that the diagrams become more complicated.

Finally, Figure 13(a) shows the transition diagram at  $Re = 16000$ . Since the transition of the topological structure of the anti-clockwise recirculating regions  $c_+^0$ ,  $c_+^1$ , and  $c_+^2$  at the cavity corners occurs asynchronously, more topologically different flow patterns appear, and the number of nodes in the transition diagram thus increases. In addition, the transitions among them also exhibit non-trivial behaviour. This is also confirmed by the fact that the eigenvalues of the transition matrix in Figure 13(b) scatter in the angular direction. According to (9), the eigenvalues whose magnitude are closer to 1 and their corresponding eigenspaces represent the slowly decaying aperiodic dynamics.

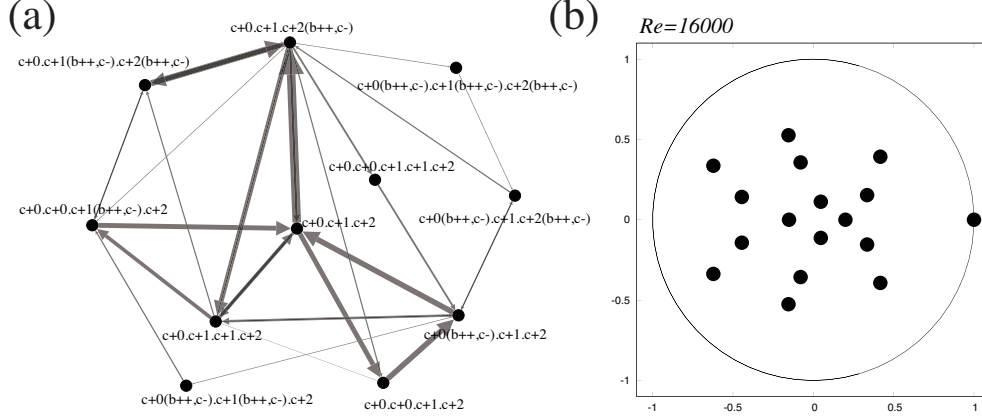


FIGURE 13. (a) Transition diagram for the evolution of the lid-driven cavity flow at the Reynolds number  $Re = 16000$ . (b) Eigenvalues of the transition matrix.

3.2.2. *Information transfer between corner regions.* This section introduces a causality-based approach to analysing flow complexity. Our graph analysis in Section 3.2.1 revealed that the discrete dynamical system's behaviour among flow patterns transitions from periodic to chaotic aperiodic states as the Reynolds number exceeds approximately  $Re = 15400$ . In periodic motions, node transitions follow a deterministic order, making it straightforward to predict pattern changes at each cavity corner. However, in aperiodic states, flow pattern changes at each corner appear asynchronous. If we interpret the order of topological changes in flow patterns at the cavity corners as information transfer resulting from flow evolution, it becomes crucial to understand how a pattern change at one corner influences changes at other corners. For example, it's not immediately apparent whether the recirculating region forms first at the top left corner  $c_+^0$  due to the uniform flow over the cavity followed by the bottom left corner  $c_+^1$ , or if the  $c_+^0$  recirculating region forms through vorticity transport from the  $c_+^1$  recirculating region via the large clockwise rotational flow in the cavity. This motivates us to investigate causality between the creation of the corner recirculating regions  $c_+^0$  and  $c_+^1$  using TFDA.

We here employ Convergent Cross Mapping (CCM) developed by Sugihara et al. [2012] to measure causality among flow pattern changes. This causal inference can be classified as observational, following the classification used for Markov processes in Baldovin et al. [2020]. This approach investigates if knowledge of one variable is useful in predicting future values of another. While interventional methods are commonly employed in fluid mechanics owing to their direct relevance to active flow control, they are unsuitable for our present analysis based on the qualitative geometric information extracted by TFDA.

To encode the instantaneous flow state based on COT, the state  $v_k^i$  of each corner  $i = 0, 1, 2$  at time  $t = t_k$  is defined as follows:  $v_k^i = 3$  if  $b_{++}$  is present inside the parenthesis of  $c_+^i$ ; otherwise, it is the smaller of the number of  $c_+^i$  and 2. We form a state vector at the  $i$ -th corner using time-delayed embedding:

$$u_k^i = (v_k^i, v_{k-\tau}^i, v_{k-2\tau}^i, \dots, v_{k-(\mathcal{E}-1)\tau}^i)$$

with  $\mathcal{E} = 30$  and  $\tau = 30$ . These values of  $\mathcal{E}$  and  $\tau$  are determined by maximising the accuracy of the autoregression. Figure 14 shows the evolution of the state vectors at the three corners by plotting the first principal components of  $u_k^i$  ( $k = 0, \dots, 5000$ ) for  $i = 1, 2, 3$  on the  $y$ -axis against time on the  $x$ -axis. Note that the unit time is 0.01. For  $Re = 14000$  (Figure 14(a)) and  $Re = 15250$  (Figure 14(b)), clear periodicity is observed, while no apparent pattern can be seen for  $Re = 15400$  (Figure 14(c)) and  $Re = 16000$  (Figure 14(d)).

To quantify spatial and temporal information transfer between corners, we quantify how accurately one local structure’s state vector predicts another’s. Since  $c_+^2$  remains static for low Reynolds numbers, we focus on the states of  $c_+^0$  and  $c_+^1$ . Using the time-delayed embedding  $u_k^i$  defined earlier, CCM evaluates prediction accuracy through correlation coefficients, using increasingly larger historical datasets until convergence. In a deterministic system, the dynamics of the driver’s variables is embedded within the effect variables’ dynamics. Higher prediction accuracy of one variable using another’s state therefore indicates that the predicted variable causally influences the predictor variable. In Figure 15, we plot two key relationships. The orange curve (“c1:c0”) shows the correlation between the predicted and actual state vectors at  $c_+^0$ , where predictions use  $c_+^1$ ’s state vector. A high correlation in this case reveals that  $c_+^0$ ’s state can be reconstructed from  $c_+^1$ ’s dynamics, indicating that  $c_+^0$  causally drives  $c_+^1$ . The blue curve (“c0:c1”) represents the reverse relationship. Up to  $Re = 15250$ , both curves maintain values near 1. It indicates an indistinguishable bidirectional causality, reflecting the periodic evolution of streamline patterns observed in Section 3.2.1. However, at approximately  $Re = 15400$ , causation from  $c_+^1$  to  $c_+^0$  (blue) weakens, while causation from  $c_+^0$  to  $c_+^1$  (orange) persists up to  $Re = 16000$ . This suggests that as Reynolds number increases, topological pattern changes at the top left corner increasingly drive changes at the bottom left corner. Notably, this causality difference between periodic and chaotic regimes, identified through our observational approach based on COT, is not captured by interventional linear response function analysis as discussed in Appendix A.

#### 4. SUMMARY

TFDA is a new method of topological data analysis for two-dimensional vector fields. It allows us to extract all local structures to be identified geometrically and to describe their global structure as a tree (COT) and its string representation (COT representation) based on the theorems by Poincaré–Hopf and Poincaré–Bendixson. Each node label (COT symbol) of the tree expresses a local orbit structure in the flow. The global configuration among local orbit structures are expressed as edges of the tree without ambiguity. Since the snapshots of the flow patterns are converted into a series of COTs or COT representations, the continuous evolution of two-dimensional incompressible flows is reduced to a discrete dynamical system between topologically equivalent flow patterns.

We apply TFDA to the evolution of the lid-driven cavity flow for the Reynolds number ranging from  $Re = 14000$  to  $Re = 16000$ , which has been well investigated as a test bed for many existing analysis methods. When the Reynolds number is  $Re = 14000$ , five topologically different streamline patterns are observed, and their corresponding COT representations repeat periodically throughout the evolution. By examining the changes in the COT representations of the flow patterns, we can theoretically identify the marginal flow pattern between them, even if it is not

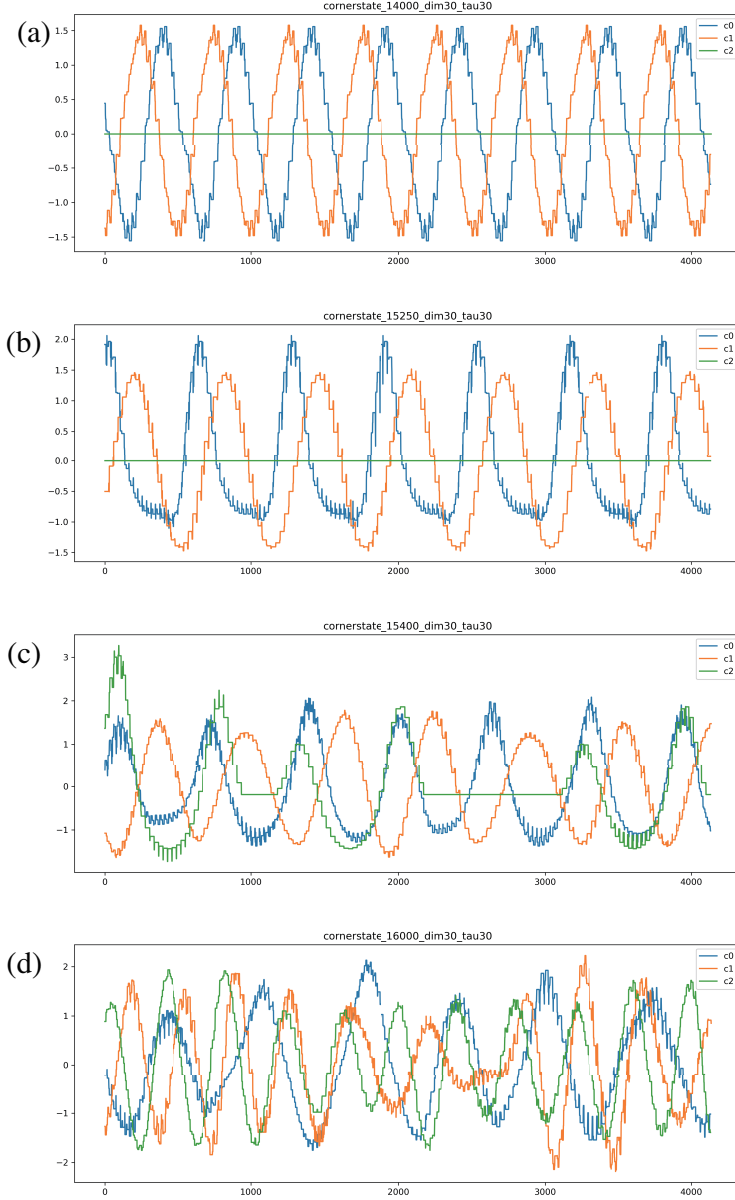


FIGURE 14. Evolution of corner states at (a)  $Re = 14000$ , (b)  $Re = 15250$ , (c)  $Re = 15400$ , and (d)  $Re = 16000$ . The plot shows the first principal component of time-delay embedded local structure states  $c_+^0$ ,  $c_+^1$ , and  $c_+^2$  at the cavity corners. The  $x$ -axis represents time, while the  $y$ -axis shows the magnitude of the first principal component. For Reynolds numbers  $Re = 14000$  and  $Re = 15250$ , we observe clear periodic behaviour in all corner states. For  $Re = 15400$  and  $Re = 16000$ , no apparent periodicity is found, indicating a transition to aperiodic flow. For  $Re = 14000$  and  $Re = 15250$ ,  $c_+^2$  remains constant, suggesting stability in this corner region at lower Reynolds numbers.

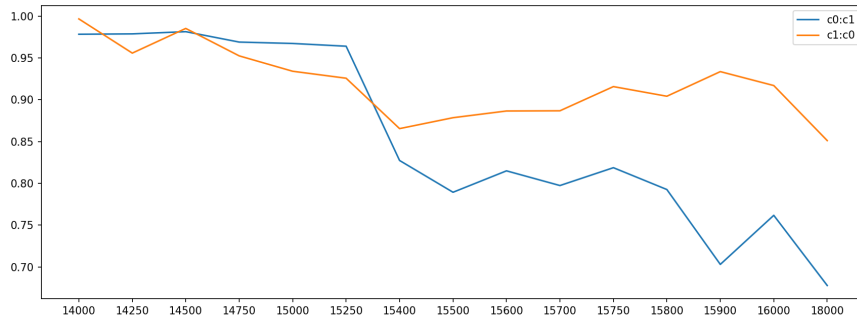


FIGURE 15. Convergent cross mapping (CCM) analysis of the corner states. The correlation coefficient between true and predicted states (the  $y$ -axis) is plotted against Reynolds number (the  $x$ -axis). The blue curve shows prediction accuracy when using  $c_+^0$  to predict  $c_+^1$ , while the orange curve shows the reverse relationship. Higher correlation coefficients indicate a stronger causal influence from the predicted state to the predictor state, following CCM theory.

explicitly contained in the simulation data. In addition, by tracking the change of the COT symbol  $c_+$  contained in the COT representations, which represent the existence of a recirculating flow domain at a cavity corner, we can express the evolution of the flow as a cyclic transition graph. Suppose that the dynamics is regarded as a Markov process on the transition graph. Then the period-five dynamics of the flow patterns are extracted as a pentagonal distribution of the eigenvalues of the transition matrix on the unit circle. This is a remarkable feature of TFDA, which describes transient pattern dynamics using the graph-theoretic approach. We apply the same analysis to the flow evolutions in the cavity from  $Re = 14000$  to  $Re = 16000$ . We find that the dynamics of the flow change from periodic to chaotic at around  $Re = 15400$ , which agrees with the critical Reynolds number confirmed by other existing analysis methods. It suggests that TFDA captures the qualitative change in the behaviour of these dynamics.

To complement our graph analysis, we employ convergence cross mapping (CCM) to investigate causal relationships between topological flow pattern changes across different cavity corners. This method analyses vectorised information from the COT representations at each corner to determine how changes in one corner's recirculating domain influence another. In the periodic flow regime ( $Re = 14000 - 15300$ ), we detect no significant causal relationships between pattern changes at different corners. However, in the chaotic regime ( $Re = 15500 - 16000$ ), we observe asymmetric causality: changes in the top left corner's topological pattern exhibit a stronger causal influence on the bottom left corner than vice versa.

TFDA's primary strengths derive from two key characteristics: robustness and interpretability. Unlike traditional methods such as POD, which are sensitive to measurement noise and numerical artefacts, COTs maintain their structural integrity under perturbations owing to their topological nature. This characteristic makes the analysis particularly reliable for experimental data where noise is inevitable. A notable example of TFDA's robustness is its application to left ventricular flows [Sakajo and Itatani, 2023], where TFDA successfully identified vortex

structures even in noisy clinical flow data obtained through echocardiography. The interpretability of COTs stems from their direct connection to physically meaningful flow structures. Each symbol in a COT corresponds to a specific qualitative feature in the flow, enabling immediate physical interpretation. This attribute contrasts with POD, where the physical meaning of individual modes occasionally remains obscure.

On the other hand, however, the COT methodology faces important limitations, particularly in its application to three-dimensional flows. The current formulation relies inherently on two-dimensional topology, necessitating the projection of three-dimensional flows onto appropriate two-dimensional sections. While this approach has proven effective in specific applications, including our analysis of left ventricular flow patterns [Sakajo and Itatani, 2023], it requires careful selection of projection planes to capture the most relevant flow features. This dimensional restriction, though limiting, often aligns well with practical applications where key flow features develop primarily in specific planes or where experimental measurements are naturally restricted to particular cross-sections. Future research directions may include extending the COT framework to a fully three-dimensional topological analysis.

#### APPENDIX A. LINEAR RESPONSE FUNCTION ANALYSIS

To highlight the differences between observational and interventional approaches in detecting causality, we present a numerical analysis of the linear response function under spatially localised forcing. This analysis provides complementary insights to the convergent cross mapping results discussed in Section 3.2.2. Let us recall the formalism of the linear response function [Marconi et al., 2008]. In the numerical simulation of the lid-driven cavity, the flow field reaches a statistically steady state such as a time-periodic state or a chaotic state at  $t = T_s$ . Then we start to add an external forcing  $f_\omega(\mathbf{x}, t)$  to the vorticity equation at this time  $T_s$  and switch it off at  $t = T_s + T_f$ . The forcing is localized in space and the duration  $T_f$  is suitably chosen, as we will discuss later. We denote the velocity and the vorticity with the forcing by  $\tilde{\mathbf{u}}$  and  $\tilde{\omega}$ . The vorticity  $\tilde{\omega}$  obeys the forced equation,

$$(10) \quad \partial_t \tilde{\omega} + (\tilde{\mathbf{u}} \cdot \nabla) \tilde{\omega} = \nu \nabla^2 \tilde{\omega} + f_\omega, \quad T_s \leq t \leq T_s + T_f.$$

We numerically solve both the forced equation (10) and the unforced vorticity equation. The velocity and the vorticity without the forcing are denoted by  $\mathbf{u}$  and  $\omega$ . If the forcing is small enough, the difference of the two vorticity fields can be expressed with the linear response function  $G_\omega(\mathbf{x}, t | \mathbf{x}', t')$  as

$$(11) \quad \Delta\omega(\mathbf{x}, t) = \tilde{\omega}(\mathbf{x}, t) - \omega(\mathbf{x}, t) = \int_{\Omega} d\mathbf{x}' \int_{T_s}^t dt' G_\omega(\mathbf{x}, t | \mathbf{x}', t') f_\omega(\mathbf{x}', t'), \quad t \geq T_s.$$

Now, for a moment, let us suppose formally that the forcing is localized at  $\mathbf{x}_f$  and  $T_s$ , that is,  $f_\omega(\mathbf{x}, t) = a\delta(\mathbf{x} - \mathbf{x}_f)\delta(t - T_s)$ , where  $\delta(x)$  is the Dirac delta function and  $a$  is the amplitude of the forcing. Then we have

$$(12) \quad a^{-1} \Delta\omega(\mathbf{x}, t; \mathbf{x}_f, T_s) = G_\omega(\mathbf{x}, t | \mathbf{x}_f, T_s), \quad t \geq T_s.$$

With this formalism, we then consider the implication of the causation in terms of the linear response function. Let us define that  $D_0$  is the region where the structure  $c_+^0$  occurs (the top left corner of the cavity) and  $D_1$  is the region where the structure  $c_+^1$  occurs (the bottom left corner of the cavity). The implication of  $c_+^1$  being more

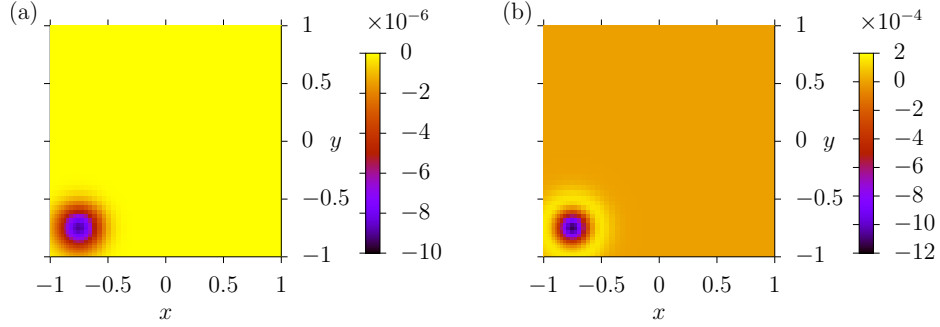


FIGURE 16. (a) The localized forcing for the streamfunction  $f_\psi(\mathbf{x}, t)$  (equation (17)), added in the region  $D_1$  ( $\mathbf{x}_f \in D_1$ ). (b) The corresponding forcing for the vorticity  $f_\omega(\mathbf{x}, t) = -\nabla^2 f_\psi(\mathbf{x}, t)$ . In the bright yellow region in the panel (b), the forcing  $f_\omega$  is positive. In other words, the profile of  $f_\omega$  is like a Mexican hat.

causal than  $c_+^0$  is that the forcing added in  $D_1$  induces larger differences than the forcing added in  $D_0$  does. Thus our anticipation is

$$(13) \quad \left| G_\omega(\mathbf{x}, t | \mathbf{x}_f, T_s) \Big|_{\mathbf{x} \in D_1, \mathbf{x}_f \in D_0} \right| < \left| G_\omega(\mathbf{x}, t | \mathbf{x}_f, T_s) \Big|_{\mathbf{x} \in D_0, \mathbf{x}_f \in D_1} \right|,$$

or equivalently,

$$(14) \quad \left| a^{-1} \Delta \omega(\mathbf{x}, t; \mathbf{x}_f, T_s) \Big|_{\mathbf{x} \in D_1, \mathbf{x}_f \in D_0} \right| < \left| a^{-1} \Delta \omega(\mathbf{x}, t; \mathbf{x}_f, T_s) \Big|_{\mathbf{x} \in D_0, \mathbf{x}_f \in D_1} \right|.$$

The linear response functions of the streamfunction can be defined likewise, and we expect that similar inequalities hold. The region  $D_0$  (the top left corner) is specifically defined as

$$(15) \quad D_0 : -1 \leq x \leq -1/2, 1/2 \leq y \leq 1,$$

and the region  $D_1$  (the bottom left corner) as

$$(16) \quad D_1 : -1 \leq x \leq -1/2, -1 \leq y \leq -1/2.$$

In practice, we do not use the delta function for the forcing, but the Gaussian function. Nonetheless, we have another problem with the locality of the forcing. If we use the Gaussian function for the vorticity forcing  $f_\omega(\mathbf{x}, t)$ , the corresponding forcing for the streamfunction  $f_\psi(\mathbf{x}, t)$  becomes much less localized. To ensure localization for both, we use the Gaussian function for the streamfunction forcing. Namely,

$$(17) \quad f_\psi(\mathbf{x}, t) = \begin{cases} \frac{a}{2\pi\sigma^2} \exp\left[-\frac{1}{2} \frac{|\mathbf{x} - \mathbf{x}_f|^2}{\sigma^2}\right], & T_s \leq t \leq T_s + T_f, \\ 0, & \text{otherwise.} \end{cases}$$

Here, the width of the forcing is set to  $\sigma = 1/8$ . We set  $\mathbf{x}_f$  either to the centre of  $D_0$  ( $(x_f, y_f) = (-3/4, 3/4)$ ), or to the centre of  $D_1$  ( $(x_f, y_f) = (-3/4, -3/4)$ ). The former case is denoted by  $\mathbf{x}_f \in D_0$  and the latter by  $\mathbf{x}_f \in D_1$ . This forcing added in the  $D_1$  region and the corresponding vorticity forcing are shown in Figure 16. Both forcings are localized. The amplitude of the forcing is set to  $a = \langle \psi \rangle_{D_j} \epsilon / \Delta t$ , where  $\Delta t$  is the time step of the simulation ( $\Delta t = 10^{-3}$  for  $Re \leq 16000$ ) and  $\langle \psi \rangle_{D_j}$



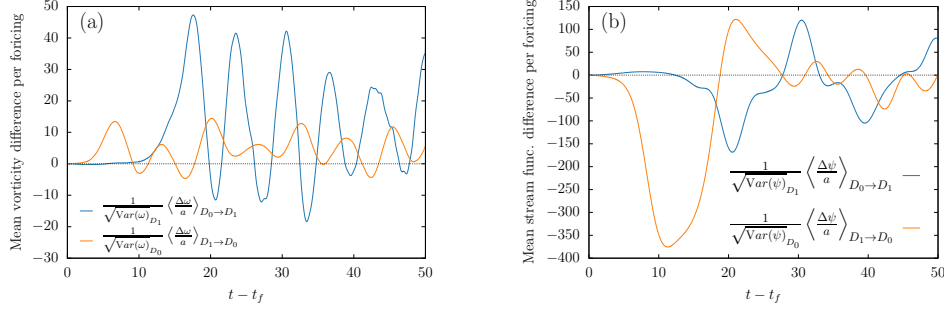


FIGURE 17. (a) The mean vorticity differences per forcing amplitude,  $a$ , as a function of time. They are proxies of the linear response functions of the vorticity. Note that the differences are also normalised by the standard deviation of the (unforced) vorticity in the observed regions. Here,  $\text{Var}(\omega)_{D_j}$  means the variance of the vorticity averaged over in the region  $D_j$  (the time average is taken as well). (b) The mean streamfunction differences. The Reynolds number is  $Re = 16000$  for both panels. The forcing is added here for  $t - T_s \leq T_f = 10$ . The differences are observed from  $t = T_s$  to  $t = T_s + 5T_f$  and the time average is taken over 100 samples of the time extent  $5T_f$ .

is the space-time average of the streamfunction without the forcing in the region  $D_j$ . We set the parameter to  $\epsilon = 1.0 \times 10^{-7}$  and check that smaller values of  $\epsilon$  than this value give the same result. The duration of the forcing is set to  $T_f = 10$ , which is about the same as the maximum delay time  $10\Delta t \times \mathcal{E} \times \tau = 9$  used for the embedding in Section 3.2.2 (recall that the COT representations are obtained at every 10 steps). We also set  $T_f$  to smaller values, e.g.,  $T_f = 0.5$ , and check that the qualitative results do not change.

In the following we observe  $a^{-1}\Delta\omega$  to check the relation (14). More specifically, we consider the average of the difference over the region  $D_1$  by adding the forcing in the region  $D_0$ , which is denoted by

$$(18) \quad \langle a^{-1}\Delta\omega \rangle_{D_0 \rightarrow D_1} = \frac{1}{(\text{Area of } D_1)} \int_{D_1} a^{-1}\Delta\omega(\mathbf{x}, t; \mathbf{x}_f, T_s + T_f) \Big|_{\mathbf{x}_f \in D_0} d\mathbf{x}.$$

Similarly we define  $\langle a^{-1}\Delta\omega \rangle_{D_1 \rightarrow D_0}$ . The average can be regarded as a suitable average of the linear response function  $G_\omega(\mathbf{x}, t | \mathbf{x}', t')$  in view of equation (11). We also calculate the difference of the streamfunction in the same manner (we only consider the scalar quantities here).

For  $Re = 16000$ , we plot the averages of the vorticity and streamfunction differences as a function of time in Figure 17. The differences are normalised by the forcing amplitude and the standard deviations of the observed regions. The amplitudes of the vorticity differences do not agree with our anticipation (13) or (14) as shown in Figure 17(a). On the other hand, for the streamfunction, with which we identified the structures  $c_+^1$  and  $c_+^0$ , the amplitude of the difference for  $D_1 \rightarrow D_0$  is non-zero in  $t \leq 15$ , while the amplitude for  $D_0 \rightarrow D_1$  is around zero,

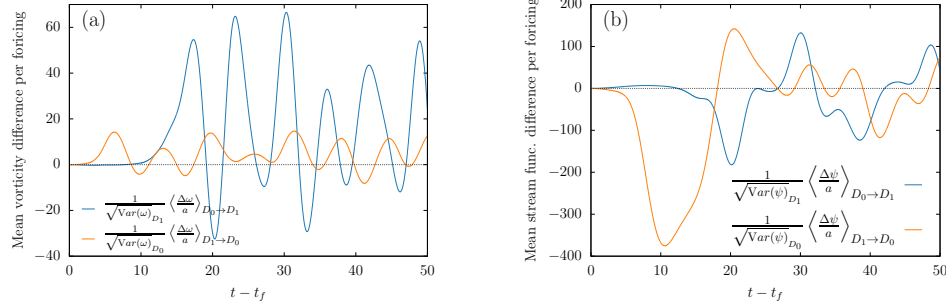


FIGURE 18. Same as Figure 17, but for  $Re = 14000$ . Those graphs are similar to the ones for  $Re = 16000$ .

as observed in Figure 17(b). However, in  $t - t_f > 15$  the amplitudes become comparable. From this behaviour, we infer that  $c_{\perp}^1$  has a causal influence on  $c_{\perp}^0$  up to around  $t - t_f = T_f$  [Baldovin et al., 2020] and that at later times no difference in causality is detected. Therefore, it is not straightforward to conclude which corner eddy is causal on another one by observing the difference of the amplitudes. For the lower Reynolds number  $Re = 14000$ , where the flow is periodic in time, we plot the averaged differences as the linear response functions in Figure 18. Their overall shapes remain similar to those for  $Re = 16000$ . Hence, we hardly find qualitative differences in linear responses across these Reynolds numbers. This may be owing to the linearity of their governing equations and comparable Péclet numbers despite the underlying flow transitioning from periodic to chaotic states. As a result, we find virtually no difference in sensitivity for periodic and chaotic evolutions. In this sense, the observational CCM approach based on TFDA can clarify the geometric causality between topological changes in flow patterns that the standard sensitivity analysis cannot capture. The discrepancy between CCM and the linear response analyses can be attributed to their fundamentally different approaches to causality detection. CCM operates in the framework of state-space reconstruction, utilising Taken’s embedding theorem to predict future states from historical time series data. In the periodic regime illustrated in Figure 10(a), the COT representations exhibit highly regular patterns. Under these conditions, the system’s future states can be predicted from any instantaneous state with equal accuracy, regardless of which corner’s information is used. This makes causal relationships appear symmetric in the CCM analysis. Linear response analysis, in contrast, provides a mechanistic view of causality by examining the system’s response to controlled perturbations. This approach directly probes the spatio-temporal propagation of disturbances through the flow field. This methodological distinction highlights the complementary nature of observational (CCM) and interventional (linear response) approaches in understanding complex fluid systems.

Finally, we discuss the relations of our work to recent studies on causality in fluid mechanics. In three-dimensional turbulent flows, a standard way is to apply POD first and then study causal relationships between the POD modes. In Lopez-Doriga et al. [2024], the square duct flow was studied to uncover the cause of the secondary flow with the POD and the Granger causality analysis. In Martinez-Snchez et al. [2023], the wake behind a circular cylinder mounted on a wall was analysed with

the POD and the entropy-transfer method for the causality. A time-series-based analysis for the sub-grid energy fluxes with different grid scales in homogeneous and isotropic turbulence was performed in Lozano-Durn and Arranz [2022] with the entropy-transfer method. The most elaborated interventional study to date in this field is Lozano-Durn et al. [2021] where the wall-bounded, minimal-flow-unit turbulence was analysed by numerically removing certain unstable modes to find the primary cause of the sustainment of the turbulent fluctuations by the mean flow. In this paper, we studied the causality between the corner eddies represented by the COT symbols  $c_+^0$  and  $c_+^1$  as discrete modes in the lid-driven cavity flow. The difference from the previous works is that we used new modes and applied both approaches of the causal analysis. The advantages of the new modes, COTs, are the immediate interpretability and the robustness to noises owing to the topological approach. The COTs are not much influenced by noise, unlike POD. The disadvantage is that it does not apply directly to three-dimensional flows, but we need to consider the projection of the flow onto an appropriate two-dimensional section as we discussed in Summary.

**Acknowledgements.** This research is supported by JST-Mirai Program Grant No. JPMJMI18G3 and JPMJMI22G1.

#### REFERENCES

- M. Baldovin, F. Cecconi, and A. Vulpiani. Understanding causation via correlations and linear response theory. *Physical Review Research*, 2(4):043436, 2020. ISSN 2643-1564. doi: 10.1103/PhysRevResearch.2.043436. URL <https://link.aps.org/doi/10.1103/PhysRevResearch.2.043436>. 3.2.2, A
- G. K. Batchelor. *An Introduction to Fluid Dynamics*. Cambridge University Press, Cambridge, UK, 1967. ISBN 978-0521663960. 2.1
- O. Botella and R. Peyret. Benchmark spectral results on the lid-driven cavity flow. *Computers & Fluids*, 27(4):421–433, May 1998. ISSN 00457930. doi: 10.1016/S0045-7930(98)00002-4. URL <http://linkinghub.elsevier.com/retrieve/pii/S0045793098000024>. 2.1, 2.1
- S. L. Brunton and J. N. Kutz. *Data-driven Science and Engineering, Machine Learning, Dynamical Systems and Control (2nd ed.)*. Cambridge University Press, 2022. 1
- H. Comon, M. Dauchet, R. Gilleron, F. Jacquemard, D. Lugiez, S. Tison, and M. Tommasi. Tree automata techniques and applications. <http://tata.gforge.inria.fr/>, 2008. URL <https://cir.nii.ac.jp/crid/1570572700056075136>. 2.3
- P. Davidson. *Turbulence An Introduction for Scientists and Engineers (2nd ed.)*. Oxford University Press, 2015. 1
- T. K. Dey and Y. Wang. *Computational Topology for Data Analysis*. Cambridge University Press, 2022. 1
- H. Edelsbrunner and J. Harer. *Computational Topology: An Introduction*. Applied Mathematics. American Mathematical Society, 2010. ISBN 9780821849255. 1
- U. Ehrenstein and R. Peyret. A Chebyshev collocation method for the Navier-Stokes equations with application to double-diffusive convection. *International Journal for Numerical Methods in Fluids*, 9(4):427–452, 1989. URL <http://onlinelibrary.wiley.com/doi/10.1002/flid.1650090405/full>. 2.1

- U. Ghia, K. Ghia, and C. Shin. High-resolutions for incompressible flow using the navier-stokes equations and a multigrid method. *Journal of Computational Physics*, 48(3):387–411, 1982. ISSN 0021-9991. doi: [https://doi.org/10.1016/0021-9991\(82\)90058-4](https://doi.org/10.1016/0021-9991(82)90058-4). URL <https://www.sciencedirect.com/science/article/pii/0021999182900584>. 2.1
- B. Lopez-Doriga, M. Atzori, R. Vinuesa, H. J. Bae, A. Srivastava, and S. T. M. Dawson. Linear and nonlinear Granger causality analysis of turbulent duct flows. *Journal of Physics: Conference Series*, 2753(1):012017, Apr. 2024. ISSN 1742-6588, 1742-6596. doi: 10.1088/1742-6596/2753/1/012017. URL <https://iopscience.iop.org/article/10.1088/1742-6596/2753/1/012017>. A
- A. Lozano-Durn and G. Arranz. Information-theoretic formulation of dynamical systems: Causality, modeling, and control. *Physical Review Research*, 4(2):023195, June 2022. ISSN 2643-1564. doi: 10.1103/PhysRevResearch.4.023195. URL <https://link.aps.org/doi/10.1103/PhysRevResearch.4.023195>. A
- A. Lozano-Durn, N. C. Constantinou, M.-A. Nikolaidis, and M. Karp. Cause-and-effect of linear mechanisms sustaining wall turbulence. *Journal of Fluid Mechanics*, 914:A8, May 2021. ISSN 0022-1120, 1469-7645. doi: 10.1017/jfm.2020.902. URL [https://www.cambridge.org/core/product/identifier/S0022112020009027/type/journal\\_article](https://www.cambridge.org/core/product/identifier/S0022112020009027/type/journal_article). A
- T. Ma and S. Wang. *Geometric Theory of Incompressible Flows with Applications to Fluid Dynamics*. American Mathematical Society, Sept. 2005. ISBN 9781470413460. doi: 10.1090/surv/119. URL <http://dx.doi.org/10.1090/surv/119>. 2.2
- U. Marconi, A. Puglisi, L. Rondoni, and A. Vulpiani. Fluctuationdissipation: Response theory in statistical physics. *Physics Reports*, 461(4-6):111–195, 2008. doi: 10.1016/j.physrep.2008.02.002. URL <http://linkinghub.elsevier.com/retrieve/pii/S0370157308000768>. A
- Martnez-Snchez, E. Lpez, S. Le Clainche, A. Lozano-Durn, A. Srivastava, and R. Vinuesa. Causality analysis of large-scale structures in the flow around a wall-mounted square cylinder. *Journal of Fluid Mechanics*, 967:A1, July 2023. ISSN 0022-1120, 1469-7645. doi: 10.1017/jfm.2023.423. URL [https://www.cambridge.org/core/product/identifier/S0022112023004238/type/journal\\_article](https://www.cambridge.org/core/product/identifier/S0022112023004238/type/journal_article). A
- R. Peyret. *Spectral Methods for Incompressible Viscous Flow*. Springer, 2002. 2.1
- A. I. Ruban and J. Gajjar. *Fluid Dynamics. Part 1. Classical Fluid Dynamics*. Oxford University Press, 2013. 1, 2.1
- T. Sakajo and K. Itatani. Topological identification of vortical flow structures in the left ventricle of the heart. *SIAM J. Imaging Sci.*, 16(3):1491–1519, 2023. doi: 10.1137/22M1536923. 1, 4
- T. Sakajo and T. Yokoyama. Transitions between streamline topologies of structurally stable hamiltonian flows in multiply connected domains. *Physica D*, 307:22–41, 2015. 3.1.1, 9
- T. Sakajo and T. Yokoyama. Tree representation of topological streamline patterns of structurally stable 2d hamiltonian vector fields in multiply connected domains. *IMA J. Appl. Math.*, 83:380–411, 2018. 1, 2.2, 2.2
- T. Sakajo and T. Yokoyama. Discrete representations of orbit structures of flows for topological data analysis. *Disc. Math. Algor. Appl.*, (2250143), 2022. 1

- T. Sakajo, Y. Sawamura, and T. Yokoyama. Unique encoding for streamline topologies of incompressible and inviscid flows in multiply connected domains. *Fluid Dynamics Research*, 46:031411, 2014. 1
- T. Sakajo, S. Ohishi, and T. Uda. Identification of kuroshio meanderings south of japan via a topological data analysis for sea surface height. *J. Oceanography*, 2022. 1
- P. N. Shankar and M. D. Deshpande. Fluid mechanics in the driven cavity. *Annual Review of Fluid Mechanics*, 32(1):93–136, 2000. doi: 10.1146/annurev.fluid.32.1.93. 2.1, 2.1
- J. Shen. Hopf bifurcation of the unsteady regularized driven cavity flow. *Journal of Computational Physics*, 95(1):228–245, 1991. URL <http://www.sciencedirect.com/science/article/pii/002199919190261I>. 1, 2.1, 2.1, 2.1, 3.2.1
- G. Sugihara, R. May, H. Ye, C.-H. Hsieh, E. Deyle, M. Fogarty, and S. Munch. Detecting causality in complex ecosystems. *Science*, 338(6106):496–500, 2012. doi: 10.1126/science.1227079. URL <https://www.science.org/doi/abs/10.1126/science.1227079>. 1, 3.2.2
- T. Uda, T. Yokoyama, and T. Sakajo. Algorithms converting streamline topologies for 2d hamiltonian vector fields using reeb graphs and persistent homology. *Trans. Japan Soc. Indust. Appl. Math.*, 29:187–224, 2019. in Japanese. 1, 2.2, 2.2, 2.3
- T. Uda, T. Sakajo, M. Inastu, and K. Koga. Morphological identification of atmospheric blockings via topological flow data analysis. *J. Meteo. Soc. Japan*, 99(5):1169–1183, 2021. 1
- T. Yokoyama and T. Sakajo. Word representation of streamline topologies for structurally stable vortex flows in multiply connected domains. *Proc. Roy. Soc. A*, 469(20120558), 2013. 1, 2.2, 2.2
- T. Yokoyama and T. Yokoyama. Cot representations of 2d hamiltonian flows and their computable applications. *in preparation*, pages 1–68, 2020. 2.3

DEPARTMENT OF MATHEMATICS, KYOTO UNIVERSITY, KYOTO, 606-8502, JAPAN  
 Email address: sakajo@math.kyoto-u.ac.jp

DEPARTMENT OF PHYSICS, KYOTO UNIVERSITY, KYOTO, 606-8502, JAPAN

INSTITUTE OF MATHEMATICS FOR INDUSTRY, KYUSHU UNIVERSITY, FUKUOKA, 819-0395, JAPAN

DEPARTMENT OF MATHEMATICS, SAITAMA UNIVERSITY, SAITAMA, 338-8570, JAPAN

ACADEMIC ASSEMBLY, UNIVERSITY OF TOYAMA, TOYAMA, 930-8555, JAPAN